12-2018

Compositional and Thermodynamic Variability in a Stratified Magma Chamber: Evidence from the Green Tuff Ignimbrite (Pantelleria, Italy).

Katarzyna M. Liszewska
University of Warsaw, kmliszewska@student.uw.edu.pl

John C. White
Eastern Kentucky University, john.white@eku.edu

Ray Macdonald
Lancaster University, r.macdonald@lancaster.ac.uk

Bogusław Bagiński
University of Warsaw, b.baginski1@uw.edu.pl

Recommended Citation

Liszewska, K.M., White, J.C., Macdonald, R., Bagiński, B., 2018, Compositional and Thermodynamic Variability in a Stratified Magma Chamber: Evidence from the Green Tuff Ignimbrite (Pantelleria, Italy). Journal of Petrology, v. 59, p. 2245-2272. doi: 10/1093/petrology/egy095

JOURNAL OF PETROLOGY

Journal of Petrology, 2018, 1–28
doi: 10.1093/petrology/egy095
Advance Access Publication Date: 29 October 2018
Original Article

OXFORD

Compositional and Thermodynamic Variability in a Stratified Magma Chamber: Evidence from the Green Tuff Ignimbrite (Pantelleria, Italy)

K. M. Liszewska[1], J. C. White[2], R. Macdonald[1,3]* and B. Bagiński[1]

[1]IGMiP Faculty of Geology, University of Warsaw, al. Żwirki i Wigury 93, 02-089 Warsaw, Poland; [2]Department of Geosciences, Eastern Kentucky University, Richmond, KY 40475, USA; [3]Environment Centre, Lancaster University, Lancaster LA1 4YQ, UK

*Corresponding author. Telephone: 0048 22772 4953. E-mail: r.macdonald@lancaster.ac.uk

Received March 23, 2018; Accepted October 11, 2018

ABSTRACT

The Green Tuff Ignimbrite, Pantelleria, is compositionally zoned from pantellerite at the base to comenditic trachyte at the top, the variation apparently representing an inverted vertical zonation in the pre-eruptive reservoir. The main phenocryst assemblages are alkali feldspar + olivine + clinopyroxene + ilmenite + apatite in the trachytes and alkali feldspar + aenigmatite + clinopyroxene ± quartz in the rhyolites. Thermodynamic modelling indicates that the temperature range was ~900–700°C, fO_2 FMQ –1·5 to FMQ –0·5 (where FMQ is fayalite–magnetite–quartz buffer) and $aSiO_2$ (relative to quartz saturation) 0·74–1·00. Melt water contents ranged from ~1 wt % in the trachytes to ~4 wt % in the pantellerites. Matrix glass analyses in the more evolved rocks are highly variable, showing that compositional layers in the upper parts of the reservoir, formed by fractional crystallization, were mixed during eruption, the proportion of rhyolitic to trachytic melts increasing towards the top of the reservoir. Some areas of glass have low Al_2O_3 contents (5·16–5·46 wt %) and high FeO* contents (9·66–10·02 wt %), making them the most evolved melts yet reported from Pantelleria. The new glass data reveal how whole-rock analyses do not truly reflect the complete range of melt compositions in the pre-eruptive reservoir. The trachytes contain >40% modal phenocrysts, which with relatively high Ba contents and positive Eu anomalies are considered to have originated in a feldspar-accumulitic layer. Phenocrysts in the trachytes are commonly heavily resorbed, inferred to be a result of heating by influxes of intermediate composition magma, which, however, were not erupted. It is argued that magmas of intermediate composition were present in the Green Tuff reservoir but were efficiently trapped in a crystal-rich layer below the Green Tuff magmas, which was eventually erupted during a resurgent phase as the Montagna Grande Trachyte.

Key words: Green Tuff ignimbrite; Pantelleria; zoned magma reservoir; magma mixing

INTRODUCTION

The rapid eruption of magma that results in the deposition of an ignimbrite frequently preserves information about the compositional structure of the magma chamber and its pre-eruptive thermodynamic state (Bachmann & Bergantz, 2008). Evidence from ignimbrites indicates that magma chambers may be (1) relatively homogeneous and lack compositional zoning (e.g. the peralkaline Gomez Tuff; Parker & White, 2008), (2) abruptly and bimodally zoned (e.g. the Mazama Tuff; Bacon & Druitt, 1988), or (3) continuously and linearly zoned (e.g. the Neapolitan Yellow Tuff; Forni *et al.*, 2018). Whether and how a magma chamber may become compositionally zoned is a complex function of both magma differentiation processes and magma chamber dynamics. Although compositional zoning is

mainly identified by whole-rock and/or phenocryst compositions, it is evident that microanalyses of glass in the same samples can reveal much greater complexity.

Peralkaline rhyolites, comendites and pantellerites, and associated trachytes are the felsic end-members of alkaline volcanism in two main tectonic settings, continental rift systems and oceanic islands. Peralkaline magmatic systems are invariably complex, showing an interplay of petrogenetic processes, such as fractional crystallization, crustal assimilation, magma mixing and remobilization of cumulate material (e.g. Bohrson & Reid, 1997; Macdonald & Scaillet, 2006; White *et al.*, 2009; Macdonald *et al.*, 2012; Jeffery *et al.*, 2017). This interplay and the additional variability raised by compositional variation (e.g. in volatile components) and tectonic setting have the result that all peralkaline systems are to some degree unique (Macdonald, 2012).

The island of Pantelleria, the type locality of pantellerite, has been of central importance in studies of peralkaline silicic magmatism. It is a composite, bimodal volcano, with alkali basalt and peralkaline rhyolite end-members. The origin of the rhyolitic magmas has been ascribed to two main mechanisms: (1) protracted fractional crystallization from an alkali basaltic parental magma (Civetta *et al.*, 1998; White *et al.*, 2005, 2009; Neave *et al.*, 2012); (2) low-degree partial melting of gabbroic cumulates to form trachyte, with subsequent fractional crystallization to generate pantellerite (Lowenstern & Mahood, 1991; Avanzinelli *et al.*, 2004; Ferla & Meli, 2006). Rocks of intermediate composition, such as mugearite and benmoreite, are rare and in many, perhaps all, cases are thought to be products of magma mixing (Ferla & Meli, 2006; Romengo *et al.*, 2012). Thus an important feature of Pantelleria is the well-defined compositional (Daly) gap.

Despite intensive study since the 1960s, some aspects of the evolution of Pantelleria remain enigmatic, including (1) the location and nature of the magma reservoir(s), (2) the genetic relationships between the mafic and silicic volcanic rocks, and (3) the detailed changes in crystallization conditions during magma evolution. The deposit termed the Green Tuff has been an important focus for addressing these, and related, problems.

(1) The Green Tuff is compositionally zoned from pantellerite to trachyte, which has been inferred to represent vertical compositional variation within the pre-eruptive magma chamber, with the pantellerites being erupted first. The zonation allows us to examine the genetic relationships between the end-members in the products of one eruption.

(2) The trachytic members show strong textural disequilibrium, which must be related to processes in the lower part of the erupted magma reservoir, such as thermal and/or compositional inputs from more mafic melts via magma mixing. This, in turn, can provide evidence for the material in the sub-trachyte part of the chamber and thus on the existence or otherwise of a Daly gap in the plumbing system.

(3) The phenocryst assemblages are suitable for estimating such parameters as temperature, fO_2 and $aSiO_2$, how they varied with melt composition and inferred depth in the magma chamber prior to eruption, and the evidence they provide for a volatile gradient.

In this study, we use whole-rock major and trace element geochemistry, groundmass glass and melt inclusion compositions, mineral chemistry, geothermometry and geochemical modelling to provide evidence for the compositional variations in the Green Tuff, the presence of a Daly gap, and the P–T–fO_2 conditions in the pre-eruptive reservoir. A significant result has been the recognition that, during eruption, the upper levels of the reservoir experienced intensive magma mixing down to the millimetre scale. Such intimate mixing has not previously been reported in peralkaline systems and indicates that the use of whole-rock analyses in studies of compositionally zoned reservoirs may not represent the full range of melt compositions.

GEOLOGICAL SETTING

Pantelleria is located in the NW–SE-trending Strait of Sicily Rift Zone (Fig. 1). The rift cuts the Pelagian Block, a promontory of the African plate. The crustal thickness under most of the block is 25–35 km, thinning to 16–17 km in the rift zone (Civile *et al.*, 2008). The Pantelleria Trough is one of three basins within the rift; it is a deep trough with a bathymetric low reaching a depth of –1317 m (Morelli *et al.*, 1975). The trough has a strong positive Bouguer anomaly (65–103 mgal; Behncke *et al.*, 2006; Civile *et al.*, 2008). It also has a high average heat flow (94 ± 21 mW m^{-2}; Verzhbitsky & Kononov, 2003), which contrasts with the continental average of 55 mW m^{-2} but is consistent with the fact that southern Italy is a hotspot in Europe, with an average of 70 mW m^{-2} (Chapman & Pollack, 1975). These features have been taken to indicate the presence of abundant basaltic magmas at depth (Della Vedova *et al.*, 1995) and asthenospheric upwelling to ~60 km, which is coincident with the maximum depth of earthquake foci that have been recorded in this area (Calò & Parisi, 2014). Little is known of the composition of the submerged part of Pantelleria. Geophysical work by Gantar *et al.* (1961) showed that it comprises a large volume of high-density rocks (3000 kg m^{-3}). By analogy with Linosa, a volcanic island some 100 km SE of Pantelleria in the Strait of Sicily, the rocks may be dominated by basalts and hawaiites (Villari, 1974). The most recent, basaltic, eruption in the area was submarine and occurred a few kilometres to the NW of the island in 1891.

At the current level of exposure, Pantelleria is dominated (~94%; Mahood & Hildreth, 1986) by trachytes and rhyolites. Eruption of basalts and hawaiites has been restricted to the northern part of the island. A well (PPT2) drilled in the northern section penetrated, at 180 m depth, more than 600 m of basaltic lavas and hyaloclastites cut by dolerite dykes (Fulignati *et al.*, 1997). A basaltic component has been recognized in mixed

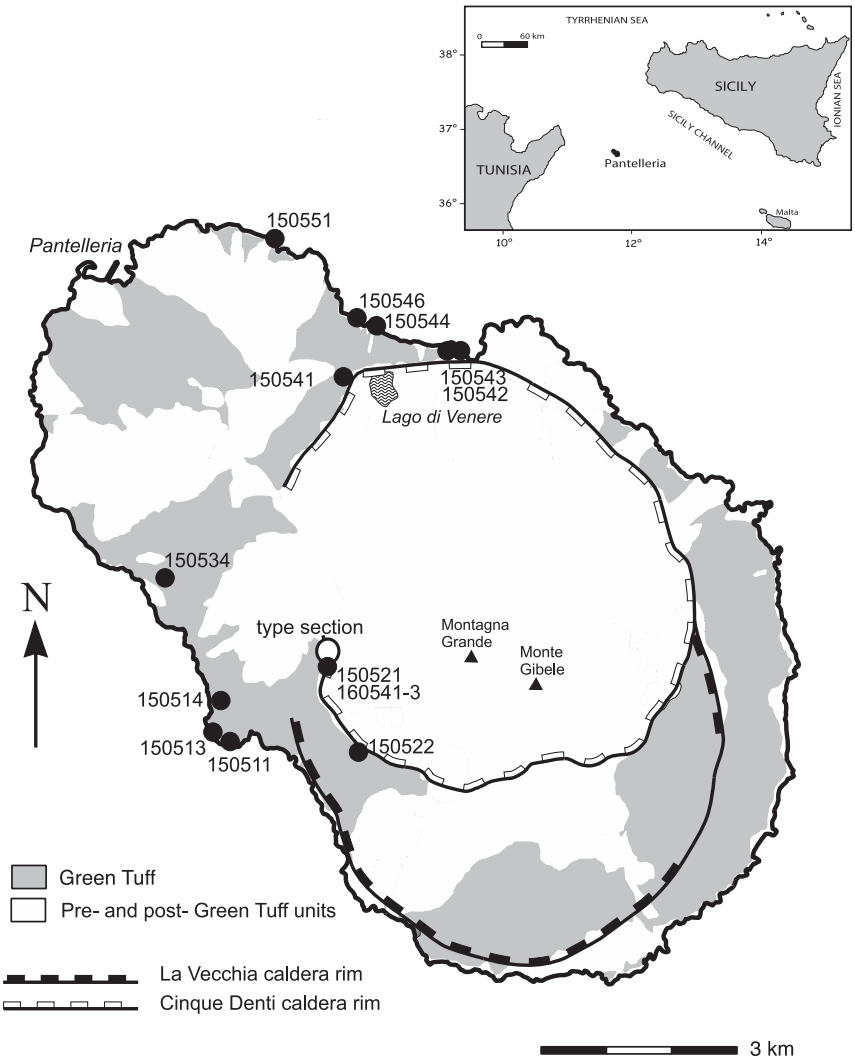

Fig. 1. Locality map showing the distribution of the Green Tuff ignimbrite and the rim faults of the La Vecchia and Cinque Denti calderas. Sample localities are indicated. Simplified from Scaillet *et al.* (2011).

magma rocks from various centres on the island, indicating the continuing presence of mafic magma at depth (Ferla & Meli, 2006; Romengo *et al.*, 2012). Magmatic activity at Pantelleria is undoubtedly basalt-driven, in that basaltic magma is the fundamental source of mass, heat and volatiles in the system.

The Green Tuff forms a thin cover over much of the 83 km^2 island, draping all topographic landforms (Fig. 1). High-precision ^{40}Ar/^{39}Ar dating has given an eruption age of 45·7 ± 1·0 ka (2σ) (Scaillet *et al.*, 2013). The volume (in dense rock equivalent; DRE) has been variously estimated as 0·28 km^3 (Jordan *et al.*, 2018), 1·5 km^3 (Civetta *et al.*, 1988), 3·5 km^3 (Mahood & Hildreth, 1986) and 7 km^3 (Wolff & Wright, 1981). The range partly reflects uncertainty in the amount of material that fell into the sea: distal ash from the eruption has been identified as far away as the Dodecanese, 1300 km east of Pantelleria (Margari *et al.*, 2007). Taking into account the offshore deposits, Margari *et al.* (2007) suggested a bulk ash volume of ∼10 km^3 DRE. The range also reflects the very variable thickness of the Green Tuff, from 30 cm to >10 m in palaeovalleys (Orsi & Sheridan, 1984). The deposit has been variously interpreted as a welded ignimbrite (Villari, 1974), a welded fall deposit (Wolff & Wright, 1981) and a sequence of pyroclastic flow units including welded fall and surge members (Orsi & Sheridan, 1984). Mahood & Hildreth (1986) described the Green Tuff as a Plinian deposit, commencing with fallout beds followed by pyroclastic flows. In the fullest, most recent study Williams *et al.* (2014) interpreted the Green Tuff as a Plinian fall deposit overlain by a single ignimbrite flow unit.

The location and nature of the eruptive sources of the Green Tuff are debatable. Following Mahood & Hildreth (1986), it has generally been accepted that eruption of the Green Tuff at 45·7 ± 1·0 ka was related to the formation of the Cinque Denti caldera (∼30 km^2), the younger of the two calderas on the island (Fig. 1). Wright (1980) argued for a central vent on the western side of the Cinque Denti caldera, whereas Mahood & Hildreth (1986) located the vent at the southern end of the caldera or in the Monte Gibele area. Williams *et al.*

(2014) suggested that the vent was on the northwestern slope of Montagna Grande. In contrast, Catalano *et al.* (2014) proposed that the tuff was erupted from fissures superimposed on NNE-trending normal fault zones within the caldera complex. They further proposed that the eruption caused only a partial collapse of the southeastern walls of the caldera, the main part of which had formed earlier, perhaps at ~87 ka. Most recently, Jordan *et al.* (2018) have argued that there have been five, or more, periods of caldera collapse on Pantelleria and that the eruption of the Green Tuff was accompanied by only partial collapse along previously established faults.

The Green Tuff is continuously zoned from comenditic trachyte at the top to pantellerite at the bottom, reflecting, in reverse order, the eruption from a zoned magma chamber (Mahood, 1984; Mahood & Hildreth, 1986; Civetta *et al.*, 1988; Williams *et al.*, 2014). Judging from the stratigraphic height versus composition profile of Williams *et al.* (2014), the trachyte forms an estimated 5–10% of the deposit. An important aspect of the Green Tuff, in terms of the evolution of Pantelleria, is that its eruption marked a peak in melt production and in the peralkalinity of the magmas, after a long intereruptive period following the 85 ka eruptive episode (Mahood & Hildreth, 1986; Scaillet *et al.*, 2013). On the basis of new $^{40}Ar/^{39}Ar$ dating and geodetic evidence of deflation and subsidence of the caldera floor, Scaillet *et al.* (2011) proposed that the intra-caldera system, in stasis since 7 ka, is on the wane and that there is no evidence of a forthcoming eruption.

Formation of the Green Tuff was followed by eruption onto the caldera floor of the volcanic rocks forming Monte Gibele (44–37 ka), which was subsequently uplifted as a resurgent block and then tilted to form Montagna Grande at ~18 ka (Fig. 1) (Mahood & Hildreth, 1986; Orsi *et al.*, 1991; Lanzo *et al.*, 2013). This edifice is composed dominantly of metaluminous trachytes, with a single recorded example of benmoreite lava (Romengo *et al.*, 2012). K–Ar dates for the trachytes overlap those of the Green Tuff, prompting Mahood & Hildreth (1986) to suggest that the trachytic activity was a continuation of the Green Tuff activity; that is, it was probably part of the same magmatic system, where continuing eruptions were a response to isostatic compensation for the material ejected during caldera formation. In contrast, Civetta *et al.* (1988) considered the Green Tuff activity to be a late-stage part of the earliest of six eruptive cycles on Pantelleria, whereas Montagna Grande was the earliest part of a second cycle. However, the existence of the six cycles has been questioned by Scaillet *et al.* (2011), partly on the basis of newer, high-precision $^{40}Ar/^{39}Ar$ ages. In the activity of the past 20 kyr, they recognized a long-term (>15 kyr) decline in eruptive frequency associated with a prominent palaeosol horizon marking a volcanic hiatus between 12 and 14 ka.

Using the joint inversion of geodetic data (levelling, EDM and InSAR), Mattia *et al.* (2007) found that the main caldera is subsiding and proposed that the measured ground deformation pattern can be explained by a simple spherical source located at ~4 km beneath the caldera. The subsidence was related to the cooling of a hydrothermal system beneath the caldera. Lanzo *et al.* (2013) combined Cl and H_2O solubility data to estimate a confining pressure of about 50 MPa (depth ~2–3 km) for the Green Tuff magma chamber, the shallow depths being consistent with petrological estimates for other pantellerite eruptions on the island (Lowenstern, 1994; White *et al.*, 2005, 2009; Di Carlo *et al.*, 2010; Neave *et al.*, 2012).

Lithostratigraphy of the Green Tuff

The Green Tuff is a very complex eruptive unit, showing major lateral and vertical heterogeneity. Primary depositional features have been obscured by various combinations of dense welding, strong rheomorphism and revesiculation. Standard methods of correlation alongstrike, such as the use of lithofacies, have proved inadequate. For example, Lanzo *et al.* (2013) divided the tuff into five members on the basis of the clearly visible variations of some megascopic features, including welding, crystal content and rheomorphic structures. Catalano *et al.* (2014) grouped the many lithofacies in the tuff into three major lithostratigraphic intervals, which show many differences in detail from the Lanzo *et al.* (2013) scheme.

In an innovative approach, Williams *et al.* (2014) used compositional variation within the deposit, as exemplified by Zr abundance, as a measure of stratigraphic height. They established a type section on the Monastero scarp (Fig. 1), which shows a continuous decrease of whole-rock Zr contents from ~2000 to 300 ppm with height within the section (Fig. 2). Lateral correlations were then made on the basis of Zr content being a time-marker during eruption of the tuff. It will be shown below that magma mixing was a significant process during eruption of the tuff, such that individual whole-rock analyses may reflect the range and proportions of mixed components. Here, it is assumed that the highest level in the reservoir being tapped by the eruption of any given magma batch is given by the highest glass Zr content in that sample. The inferred positions of samples are consistent with the field occurrence, where known; for example, the basal pumice fall, basal vitrophyre and upper vitrophyre (Fig. 2).

SAMPLING AND ANALYTICAL METHODS

The aims of this study included determining the range of melt compositions in the Green Tuff, and studying in detail the melt–phenocryst relationships. It was critical, therefore, that, wherever possible, pristine melt (glass) compositions were determined. The only previous study to focus on glass compositions in the Green Tuff is that of Williams *et al.* (2014). However, as they acknowledged, the beam diameter used in their laser

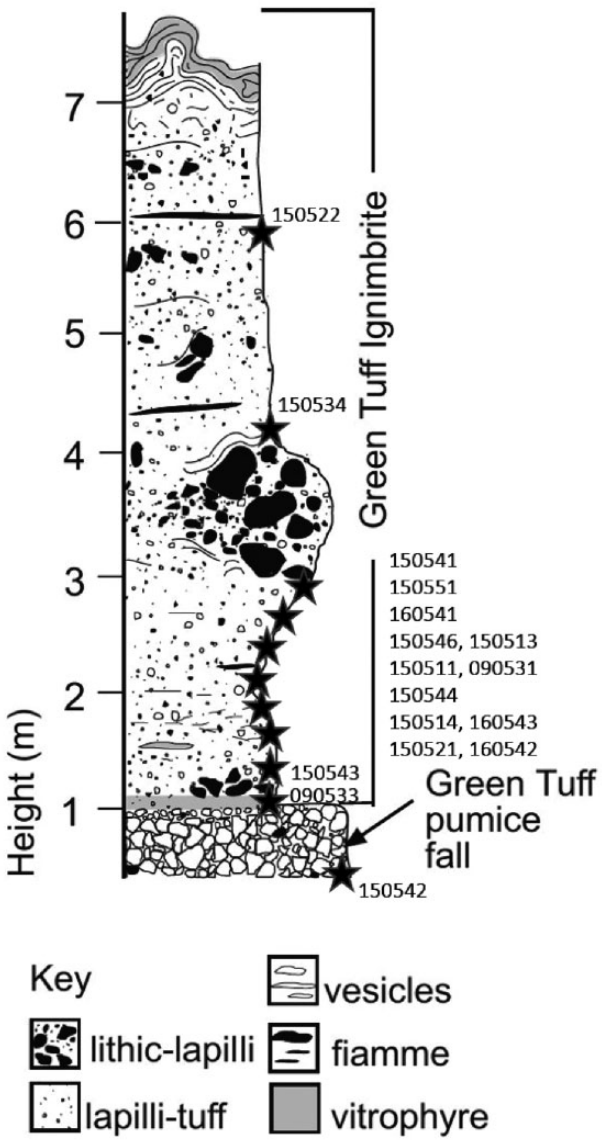

Fig. 2. Vertical section through the Green Tuff pumice fall and ignimbrite at the type locality on the Monastero scarp where it is ~7·5 m thick. Modified from Williams *et al.* (2014). The trachytic component is found in the rheomorphic vitrophyre at the top of the deposit (wavy lines). Approximate positions of our samples within the stratigraphy are shown.

ablation inductively coupled plasma mass spectrometry (LA-ICP-MS) determinations was sufficiently large that their analyses probably included glass and microlites. The electron microprobe technique used here allowed us to focus on areas of clean glass, although the presence of submicroscopic microlites cannot be excluded in every case. Samples were collected from 15 localities (Appendix). Glass was found in 11 samples (Table 1); certain facies of the tuff, especially strongly welded and trachytic varieties, are completely devitrified. A small number of analyses of glass inclusions in phenocrysts were also made.

Two whole-rock analyses (samples 090531 and 090533) were made at Activation Laboratories, Ancaster, Ontario, for major elements and Cu, Ni, Pb and Zn by inductively coupled plasma atomic emission spectrometry (ICP-AES) (Code 481) and other trace elements by ICP-MS (Code 4Lithoresearch), F by ion selective electrode (Code 4F-F) and Cl by instrumental neutron activtion analysis (INAA) (Code 4F-Cl). A further 15 whole-rock analyses were made at Bureau Veritas Commodities Canada Ltd (Table 2). Major elements and Cr were analysed by ICP-AES, and trace elements, including rare earth elements (REE), by ICP-MS. Mean detection limits on major elements were close to 0·1 wt %, whereas the detection limits for trace elements varied from 0·01 to 0·1 ppm.

Mineral compositions were determined by electron microprobe at the Inter-Institute Analytical Complex at the Institute of Geochemistry, Mineralogy and Petrology, University of Warsaw, using a Cameca SX-100 microprobe equipped with four wavelength-dispersive spectrometers. The analytical conditions for minerals, except feldspar, were accelerating voltage 15 kV and probe current 20–40 nA, with counting times of 20 s on peak and 10 s on each of two background positions. For feldspar, a beam spot diameter of 5 μm was used, to reduce Na loss. For glass analyses, 15 kV and 6–10 nA and a defocused spot of ~10–20 μm were used. Certain problems can arise with analysis of glass. As well as compositional variations related to incomplete mixing of melts, the melts may have been heterogeneous because of (1) proximity to different phenocrysts and (2) contamination by microlites. In our experience, for example, contamination by feldspar and FeTi-oxide microlites can cause some scatter in Fe and Al abundances. We have attempted to mitigate these problems by analyzing clear pools of matrix glass as far as possible from phenocryst phases.

The 'PAP'φ(ρZ) program (Pouchou & Pichoir, 1991) was used for corrections. Apatite was analysed using the technique outlined by Macdonald *et al.* (2008). Estimates of analytical precision (1σ; wt %) for all phases except glass are Si 0·07, Ti 0·03, Al 0·02, Cr 0·02, Ni 0·03, Fe 0·09, Mn 0·03, Mg 0·04, Ca 0·08, Na 0·01 and K 0·01. For glass analyses, the values are Si 0·40, Ti 0·03, Al 0·14, Fe 0·29, Mn 0·12, Mg 0·02, Ca 0·03, Na 0·17, K 0·11, P 0·03, Zr 0·08, Cl 0·03 and F 0·08. The numbers of point analyses obtained for phenocrysts were alkali feldspar 501, fayalite 102, hedenbergite 171, FeTi-oxides 27, aenigmatite 58 and apatite 10; for matrix glass and melt inclusions the number of point analyses was 145. Representative glass analyses are given in Table 3; the full phenocryst and glass dataset is given in Supplementary Data Electronic Appendices 1–3; supplementary data are available for downloading at http://www.petrology.oxfordjournals.org.

PETROGRAPHY

Phenocryst assemblages

Phenocryst assemblages are reported in Table 1. Alkali feldspar phenocrysts are present in all samples, their

Table 1: Phenocryst and glass compositions

Sample	Whole-rock	Phenocryst compositions								Glass composition ranges	
		alk feldspar Or%	olivine Fo%	clinopyrox. En%	aenigmat. Ca + Al	ilmenite X_{ilm}	magnetite X_{usp}	quartz	apatite REE + Si	SiO_2 wt %	ZrO_2 wt %
150511	p	33·5–36·3	—	7·8–9·4	0·19–0·23	—	—	—	—	69·8–71·0	0·23–0·37
150513	p	23·2–36·6	6·2–9·3	8·4–12·2	—	94·7–95·4	46·7–49·0	—	0·17	67·9–71·3	0·23–0·35
150514	p	26·6–36·2	—	8·1–12·6	0·18–0·23	96·8–98·3	—	+	+	70·0–72·7	0·23–0·40
150521	p	34·6–37·8	—	8·2–10·4	0·16–0·21	—	—	—	+	64·8–73·7	0·23–0·35
150522	ct	19·1–35·4	+	26·1–28·8	—	+	—	+	0·06	60·0–64·9	b.d.–0·18
150534	p	31·1–36·5	9·5–13·5	8·8–13·3	0·15–0·20	96·3–96·8	70·0–76·0	—	+	64·8–72·9	0·12–0·37
150541	ct	20·1–33·1	15·1–15·8	12·8–21·7	—	+	66·5–73·5	+	0·10–0·24	—	—
150542	p	+	—	+	+	+	—	—	—	69·6–72·1	0·23–0·38
150543	p	+	—	+	+	+	—	—	—	70·1–71·7	0·21–0·35
150544	p	33·0–36·9	—	8·2–11·5	0·16–0·18	+	—	—	+	70·0–73·5	0·23–0·43
150546	p	33·9–35·9	—	8·8–11·2	0·26–0·27	+	—	—	+	69·8–72·7	0·22–0·36
150551	p	29·4–35·9	7·0–12·8	12·3–22·2	0·26–0·27	97·6–98·6	—	—	+	66·7–71·1	b.d.–0·40
160541	p	33·4–35·5	9·3	43·1–49·6	0·16–0·22	95·6–96·9	—	—	0·16–0·24	—	—
160543	p	34·9–35·7	—	+	+	—	—	?	+	—	—

p, pantellerite; ct, comenditic trachyte [classification scheme of Macdonald (1974)]; +, present but not analyzed, b.d., below detection.

abundance ranging from 30–40 modal % in the comenditic trachytes to <10 modal % in the pantellerites. Mafic phenocrysts are much less abundant, normally occurring in total in amounts less than 5 modal %. Exceptions are clinopyroxene in sample 150521 (~5%) and aenigmatite in 150514 (~2–3%).

Whereas the alkali feldspar phenocrysts in the rhyolites tend to be euhedral to subhedral, homogeneous and up to 3 cm across, those in the trachytes are commonly highly resorbed (see Korringa & Noble, 1972; Troll & Schmincke, 2002; Romengo *et al.*, 2012; D'Oriano *et al.*, 2017; Fig. 3a and b). Resorbed and euhedral crystals are sometimes present together in mixed magma rocks. Olivine phenocrysts occur in the less peralkaline rocks, commonly showing highly resorbed textures (Fig. 3c). Clinopyroxene is ubiquitous, varying in form from perfectly euhedral to partially resorbed plates (Fig. 3d). Zoning is common, marked by differing shades of green.

Quartz phenocrysts are rounded and up to 1 cm in size. They are found only in the more peralkaline host glasses and appear to have been of relatively late crystallization, consistent with the observation of Di Carlo *et al.* (2010) from their experimental work on Pantescan pantellerites. Aenigmatite phenocrysts, most commonly forming euhedral prisms, are also restricted to the more peralkaline hosts. Ilmenite occurs throughout the whole-rock compositional range, commonly in association with clinopyroxene and olivine but also as discrete subhedral crystals. Titanomagnetite is scarcer and more texturally variable: it is present as equant microphenocrysts, forms rims to ilmenite phenocrysts and occurs as tiny crystals along the rims of melt inclusions. Exsolution lamellae are occasionally observed. Apatite microphenocrysts occur over the complete whole-rock compositional range, although they are most abundant in the trachytic members. They most commonly form euhedral prismatic crystals, up to a few tens of micrometres long, associated with clinopyroxene and olivine phenocrysts. Pyrrhotite occurs in most samples, usually as small crystals (<20 μm) enclosed in olivine and clinopyroxene phenocrysts.

As noted above, many samples contain glass of more than one composition and the phenocryst assemblages reflect those compositional ranges. Taking this into account, some general observations of phenocryst distribution can be made. The two dominant assemblages are (1) alkali feldspar + fayalite + hedenbergite + ilmenite + apatite and (2) alkali feldspar + hedenbergite + aenigmatite ± ilmenite ± quartz + apatite. Assemblage (2) occurs in the more peralkaline rocks and (1) in the more trachytic types. Samples containing phases more commonly found in melts of slightly different composition (e.g. fayalite and aenigmatite in samples 150534 and 150551; Table 1) contain glass of more than one composition and the phenocryst assemblages may reflect those compositional ranges. However, it will be shown below that the assemblage fayalite + ilmenite + aenigmatite may be in equilibrium under very specific conditions.

Glass

The majority of samples contain two or more varieties of glass, the relationships between them being very variable. In some cases, the glasses have different colours in plane-polarized light, reflecting differing degrees of devitrification or microvesicularity without significant compositional differences. In others, the colours reflect magma mixing, which takes several forms. In Fig. 4a rounded blobs of black glass are mingled with a pale brown type. Both types contain alkali feldspar phenocrysts. Figure 4b shows streaky intermingling of dark brown and pale glasses, feldspar phenocrysts being more common in the dark variety. Slightly denser welding in Fig. 4c has resulted in mingling of narrow

Table 2: Whole-rock compositions of Green Tuff, Pantelleria

Sample:	150511	150513	150514	150521	150522	150534	150541	150542	150543	150544	150546	150551	160541	160542	160543	090531	090533
Rock (L):	R	T	T	R	T	T	T	T	T	T	T	T	R	R	R	R	R
Rock (M):	P	P	P	P	CT	P	C	P	P	P	P	P	P	P	P	P	P
wt%																	
SiO_2	69·22	68·78	67·51	69·07	64·68	65·59	67·34	67·55	68·84	67·99	68·07	67·02	69·51	69·33	69·37	70·16	69·19
TiO_2	0·50	0·52	0·51	0·50	0·69	0·59	0·47	0·51	0·54	0·51	0·53	0·54	0·48	0·50	0·50	0·53	0·54
Al_2O_3	9·27	9·71	9·38	9·39	15·21	12·14	13·88	8·90	9·14	9·69	10·19	12·08	11·39	9·05	9·10	8·95	9·29
FeO*	7·74	7·68	7·46	7·51	5·29	6·87	4·88	7·61	8·06	7·67	7·55	6·61	6·39	7·73	7·74	8·68	9·01
MnO	0·29	0·29	0·28	0·28	0·21	0·26	0·22	0·29	0·30	0·29	0·28	0·26	0·25	0·29	0·29	0·29	0·30
MgO	0·13	0·19	1·36	0·12	0·47	0·27	0·23	0·21	0·14	0·16	0·14	0·17	0·25	0·11	0·12	0·22	0·20
CaO	0·42	0·46	0·52	0·41	1·23	0·66	0·67	0·42	0·43	0·43	0·47	0·62	0·44	0·39	0·42	0·48	0·49
Na_2O	6·42	6·29	4·97	6·25	6·31	6·09	5·90	5·39	6·34	6·43	6·39	6·42	5·08	6·51	6·03	5·46	5·09
K_2O	4·60	4·68	4·46	4·62	4·57	4·68	4·92	4·56	4·62	4·60	4·67	4·88	4·91	4·62	4·58	4·50	4·63
P_2O_5	0·03	0·03	0·04	0·03	0·15	0·04	0·05	0·04	0·03	0·03	0·03	0·03	0·03	0·03	0·03	0·07	0·03
F	0·12	0·11				0·08	0·08	0·12	0·18		0·13	0·09				0·05	0·08
LOI	0·10	0·10	2·20	0·50	0·20	1·80	0·60	3·20	0·20	0·90	0·40	0·30	0·20	0·10	0·50	−0·10	0·04
Sum	98·84	98·84	98·69	98·68	99·01	99·07	99·24	98·80	98·82	98·70	98·85	99·02	98·93	98·66	98·68	99·29	98·89
O = F	0·05	0·05				0·03	0·03	0·05	0·08		0·05	0·04				0·02	0·03
Total	98·79	98·79	98·69	98·68	99·01	99·03	99·20	98·75	98·75	98·70	98·79	98·99	98·93	98·66	98·68	99·27	98·86
Total C	0·03	0·02	0·05	0·04	0·07	0·03	0·05	0·10	0·02	0·05	0·03	0·03	0·03	0·05	0·04		
Total S	0·03	0·04	0·04	0·03	b.d.	0·02	<0·02	<0·02	0·03	0·04	0·03	0·03	b.d.	0·03	0·03	0·01	0·01
ppm																	
Ba	60	80	61	64	1893	153	380	61	52	73	86	148	16	52	62	74	71
Be	4	11	10	13	2	3	4	18	9	8	11	5	6	8	8	12	9
Co	0·5	0·3	0·5	0·2	1·7	0·5	0·4	0·4	0·3	0·3	0·6	0·5	0·3	0·2	0·5	< 0·1	< 0·1
Cs	1·5	1·6	0·2	2	0·2	1·2	0·2	2·5	2·0	1·9	1·8	1·1	0·3	1·8	2·1	1·1	< 0·2
Ga	30·8	32·0	34·9	33·2	31·3	34·1	32·9	30·8	32·6	32·8	34·6	37·1	33·9	34·7	33·6		
Hf	36·8	34·9	38·9	39·1	13	20·8	21·5	39·6	37·8	39	33·9	24·1	34·4	41·0	39·6	39·1	39·8
Nb	286	283·1	310·3	314·2	112·1	196·3	185	313·1	315·9	296·8	274·8	206·2	265·5	315·1	306·9		
Rb	151·1	143·9	114·1	170·7	66	100·6	93·6	160·1	160·8	157·9	142·1	110·8	145·8	170·7	166·0	180	160
Sc	3	3	3	4	10	6	4	3	3	3	4	5	6	3	3	4·1	4·4
Sn	24	12	16	12	8	19	7	12	16	13	12	15	8·0	12·0	12		
Sr	3·3	4·7	29·2	4·3	65·4	8·1	21·7	8·3	3·3	7·7	5·1	6·0	2·4	2·8	4·3	10	8
Ta	17·0	16·5	18·3	18·3	6·5	11·4	10·5	19·0	18·5	19·5	16·7	12·2	17·3	19·9	18·8	20·4	21·8
Th	28·1	27·6	30·1	31·5	10·8	17·4	17·0	31·5	30·0	30·4	26·7	18·4	27·4	32·3	31·3	34·8	32·2
U	8·7	8·8	3·1	9·8	1·3	4·7	1·4	9·6	9·3	9·4	7·8	5·4	5·2	10·2	9·3	7·7	4·5
W	4·1	4·5	1·6	4·5	1·3	2·6	1·4	4·7	4·5	4	3·8	2·8	1·1	5·0	4·9	<1	8
Zr	1582·2	1537·9	1673·8	1718·1	552·5	967·5	1010	1760·6	1736·3	1633·7	1502·9	1047·7	1451·3	1725·2	1689·9	1589·0	1740·0

(continued)

Table 2: Continued

Sample:	150511	150513	150514	150521	150522	150534	150541	150542	150543	150544	150546	150551	160541	160542	160543	090531	090533
Rock (L):	R	T	T	R	T	T	T	T	T	T	T	T	R	R	R	R	R
Rock (M):	P	P	P	P	CT	P	C	P	P	P	P	P	P	P	P	P	P
Y	141·6	136·0	144·3	147·1	50·5	85·0	64·7	161·7	146·5	136·3	130·3	94·0	53·1	146·9	140·0	129·0	100·0
La	188·1	184·7	207·8	203·2	84	116·6	127·3	213·8	207·3	191·8	174·5	135·1	146·6	212·2	204·7	206·0	202·0
Ce	352·2	344·9	377·6	383·3	152·4	214·5	198·5	376·0	375·8	373·2	324·9	244·1	269·7	394·8	394·9	309·0	318·0
Pr	41·91	38·45	40·76	41·57	17·97	25·73	26·81	43·46	41·62	39·43	36·85	28·12	26·94	42·05	41·32		
Nd	143·0	138·5	145·8	147·4	67·3	93·7	100·6	159·4	151·1	138·7	132·1	103·2	92·2	153·7	146·2	135·0	138·0
Sm	27·72	26·86	28·48	28·76	12·68	18·52	17·76	31·22	29·93	27·11	26·38	20·31	14·94	29·24	28·63	23·90	23·60
Eu	4·14	4·20	4·46	4·41	4·38	3·16	3·02	4·71	4·51	4·1	4·13	3·46	1·82	4·45	4·33	4·34	4·35
Gd	25·96	25·17	26·42	26·55	11·74	16·81	15·17	29·4	27·76	24·94	24·54	18·82	11·65	26·92	25·87		
Tb	4·44	4·32	4·42	4·40	1·83	2·81	2·52	5·00	4·74	4·21	4·22	3·11	1·81	4·52	4·40	3·30	3·40
Dy	25·72	25·91	26·36	27·04	10·29	16·42	14·19	29·41	28·27	25·73	24·57	18·28	10·70	26·99	26·89		
Ho	5·14	4·97	5·46	5·64	2·03	3·12	2·55	5·79	5·51	5·21	4·68	3·52	2·03	5·60	5·39		
Er	15·65	15·03	15·25	15·92	5·31	9·34	7·36	17·84	17·05	15·08	14·36	10·54	6·46	15·99	15·61		
Tm	2·21	2·16	2·28	2·28	0·78	1·35	1·08	2·59	2·36	2·18	2·06	1·46	1·02	2·27	2·28		
Yb	13·80	13·97	14·57	14·29	4·92	8·99	7·70	16·08	15·00	13·70	13·46	9·87	7·38	14·93	14·55	13·30	12·00
Lu	2·07	1·98	2·10	2·10	0·68	1·27	1·11	2·33	2·26	2·01	1·94	1·43	1·18	2·18	2·09	1·95	1·78
PI	1·68	1·59	1·39	1·63	1·01	1·24	1·08	1·55	1·69	1·61	1·53	1·31	1·20	1·74	1·63	1·55	1·44
Eu/Eu*	0·45	0·47	0·48	0·47	1·08	0·53	0·54	0·46	0·46	0·47	0·47	0·52	0·41	0·47	0·47	0·56	0·57
[La/Yb]	9·78	9·48	10·23	10·20	12·25	9·30	11·86	9·54	9·91	10·04	9·30	9·82	14·25	10·19	10·09	10·44	11·35
[Tb/Yb]	1·46	1·41	1·38	1·40	1·69	1·42	1·49	1·41	1·44	1·40	1·43	1·43	1·11	1·38	1·37	1·09	1·25

p, pantellerite, c, comendite, ct, comenditic trachyte [classification scheme of Macdonald (1974)]. T, trachyte, r, rhyolite [total alkalis–silica (TAS) scheme; Le Maitre, 2002]. PI, peralkalinity index [molar $(Na_2O + K_2O)/Al_2O_3$]. LOI, loss on ignition. Blanks, not determined.

Table 3: Representative compositions of matrix glasses and melt inclusions in Green Tuff

wt %	1	2	3	4	5	6	7	8	9	10	11	12
SiO_2	69·96	62·84	63·04	64·79	71·49	67·27	71·90	70·98	66·72	70·68	72·52	72·74
TiO_2	0·46	1·07	0·72	0·40	0·48	0·47	0·42	0·49	0·69	0·52	0·73	0·72
ZrO_2	0·27	b.d.	b.d.	b.d.	b.d.	0·12	0·33	0·43	0·11	0·25	0·40	0·28
Al_2O_3	7·86	14·10	14·64	15·16	9·72	11·15	8·05	7·63	11·68	7·87	5·31	5·45
FeO*	8·30	7·02	5·89	4·33	5·39	7·37	7·75	8·05	7·40	7·65	9·93	9·66
MnO	0·32	0·19	0·17	0·14	0·15	0·15	0·42	0·31	0·27	0·31	0·45	0·31
MgO	0·09	0·44	0·35	0·72	0·72	0·23	0·12	0·09	0·16	0·11	0·13	0·15
CaO	0·34	1·74	1·24	0·68	0·80	1·63	0·27	0·26	0·42	0·37	0·46	0·36
Na_2O	6·26	7·00	6·86	6·68	6·06	6·20	5·84	6·38	6·55	6·11	5·60	5·64
K_2O	4·58	4·56	5·24	5·58	3·14	4·14	3·41	4·53	4·92	4·55	4·29	4·27
P_2O_5	b.d.	0·26	0·11	b.d.	b.d.	b.d.	b.d.	b.d.	b.d.	b.d.	b.d.	b.d.
Cl	0·93	0·07	b.d.	0·07	0·07	0·34	1·16	0·99	0·52	0·86	1·05	0·99
SO_3	0·06	0·07	0·08	0·04	0·06	0·07	0·07	0·10	0·09	0·08	0·16	0·11
Sum	99·43	99·36	98·34	98·59	98·08	99·14	99·74	100·24	99·53	99·36	101·44	101·43
O = Cl	0·21	0·02	0·00	0·02	0·02	0·08	0·27	0·23	0·12	0·20	0·24	0·23
Sum	99·22	99·34	98·34	98·57	98·06	99·06	99·47	100·01	99·41	99·16	101·20	101·20
PI	1·94	1·17	1·16	1·12	1·38	1·32	1·65	2·02	1·38	1·90	2·61	2·55

Explanation: 1, pale brown glass, sample 150511; 2, dark bleb, 150522; 3, melt inclusion in feldspar, 150522; 4, 5, black blebs of glass, 150534; 6, pale glass, 150534; 7, brown glass, 150542; 8, grey speckled glass, 150544; 9, 10, brown glass, 150551; 11, 12, melt inclusions in feldspar, 150514. FeO*, all Fe as Fe^{2+}. b.d., below detection. PI, peralkalinity index [molar $(Na_2O + K_2O)/Al_2O_3$].

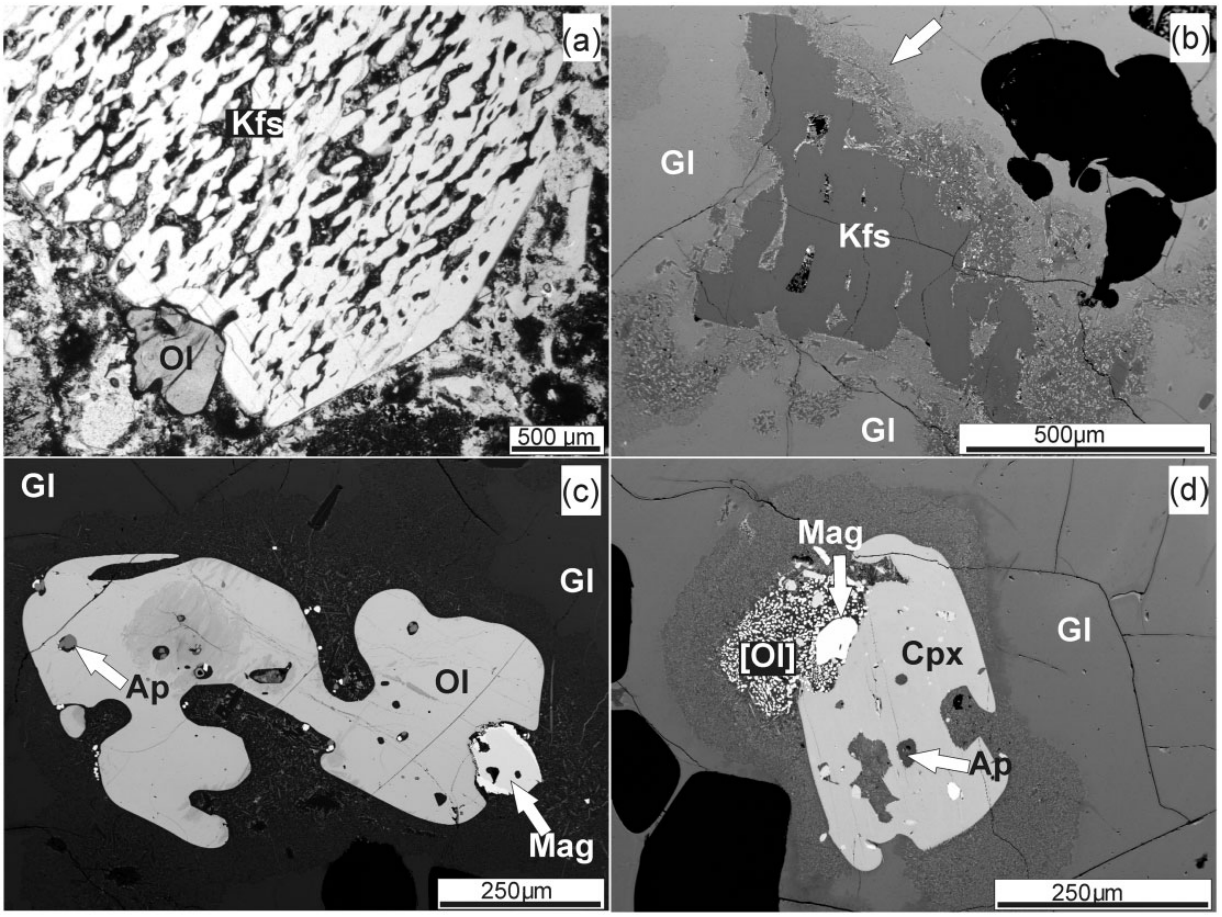

Fig. 3. Resorption of phenocrysts in trachytic host rocks. (a) Sieve-texture in alkali feldspar (Kfs). The small phenocryst is fayalite (Ol). Sample 150522. (b) Heavily resorbed alkali feldspar in 150513. The darkening and incipient devitrification of the glass (Gl) around the crystal (arrowed) should be noted. (c) Fayalite phenocryst (Ol), with apatite (Ap) inclusion. The crystal partially includes a magnetite microphenocryst (Mag). Sample 150513. (d) Partially resorbed hedenbergite phenocryst (Cpx; 150513), containing inclusions of apatite and magnetite. The associated phenocryst is fayalite, completely replaced by magnetite + quartz. The darkening and incipient devitrification of the glass around the crystal should be noted. Details of the samples are given in the Appendix.

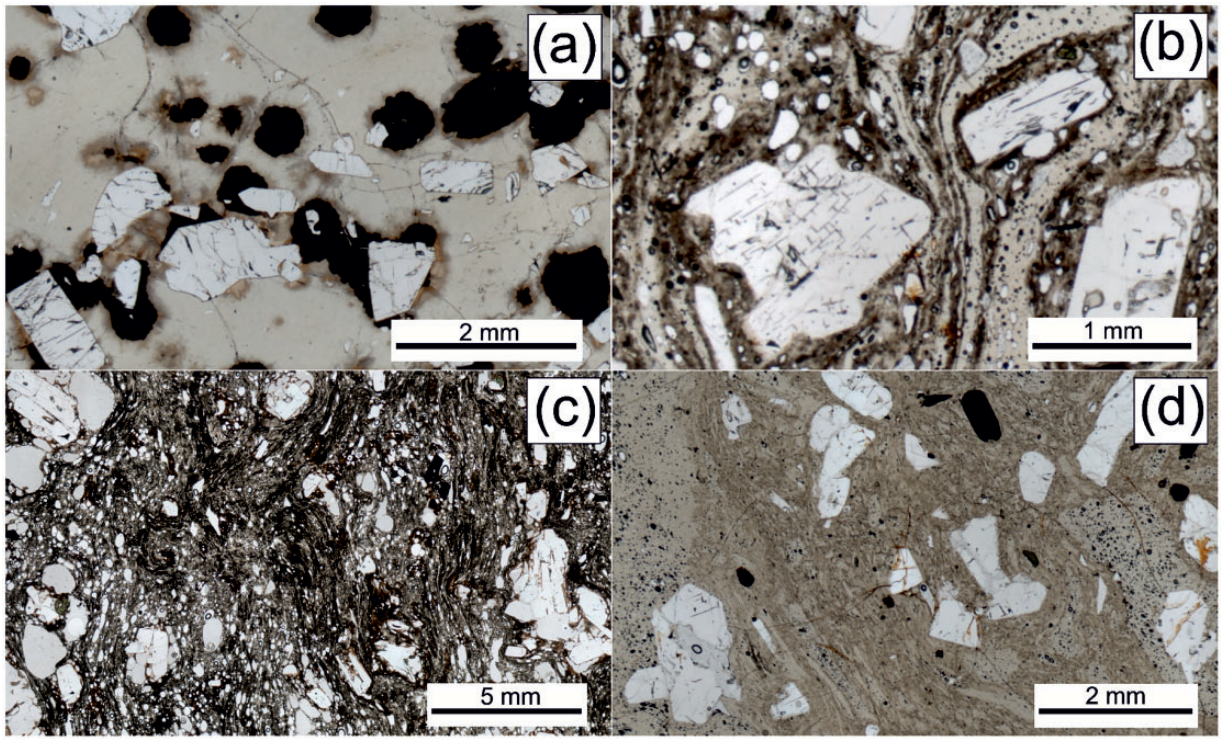

Fig. 4. Different styles of magma mixing in the Green Tuff. (a) Round blebs of dark glass embedded in pale brown glass. Alkali feldspar crystals (Kfs) occur in both types. Sample 150513. (b) Densely welded tuff with intermingled dark brown and pale fiamme. Sample 150551. (c) Densely welded type with mingling of at least two varieties of glass. Sample 150543. (d) A less densely welded sample shows pale and slightly deeper brown glasses streakily intermingled along their junction. A euhedral aenigmatite phenocryst is present at top centre. Sample 150544. Details of the samples are given in the Appendix.

fiamme, the paler type being more devitrified. The less densely welded sample in Fig. 4d shows pale and slightly deeper brown glasses patchily intermingled along their junction. No relationship between the type of mixing and height within the deposit has been discerned.

Apart from two point analyses in clinopyroxene, all analyses of melt inclusions were made in alkali feldspar phenocrysts (Supplementary Data Electronic Appendix 3). The inclusions are similar to those described from the Green Tuff by Lanzo *et al.* (2013); the dominant forms are ovoid and subspherical, up to 250 μm across. The analysed inclusions are composed entirely of glass.

PHENOCRYST COMPOSITIONS

Alkali feldspar

Alkali feldspar phenocrysts are anorthoclase, in the compositional range $An_{10}Ab_{70}Or_{20}$ to $An_{0}Ab_{63}Or_{37}$, with an outlier at Or_{40} (Supplementary Data Electronic Appendix 1a). The Or and Fe contents generally increase with whole-rock peralkalinity. Barium contents ($\leq$0·01 a.p.f.u.) are detectable only in feldspars with CaO >0·5 wt %. The compositional range within samples is usually small; for example, in 150511, 150546 and 150551 the range is Or <3. In others (e.g. 150541) a slightly larger range ($An_{6·2}Ab_{73·5}Or_{20·3}$ to $An_{0·2}Ab_{68·2}Or_{31·8}$) reflects phenocryst occurrence in glasses of different composition. With the exception of those with higher CaO contents (>0·6 wt %), all the alkali feldspar phenocrysts have peralkalinity indices [PI = molar $(Na_2O + K_2O)/Al_2O_3$] in the range 1·0–1·14.

Olivine

Olivine phenocryst compositions are in the range $Fo_{6–25}$, the Fo content decreasing with increasing whole-rock peralkalinity (Supplementary Data Electronic Appendix 1b). They show high abundances of MnO (3·7–4·6 wt %). Calcium contents are moderate, $\leq$0·75 wt % CaO, and show a positive correlation with Fo, except for sample 150541 in which the olivines are relatively Ca-poor. Zoning is generally weak, <1% Fo, except for one strongly resorbed crystal in 150513 where the range is $Fo_{9·8–6·3}$.

Clinopyroxene

Clinopyroxene phenocrysts are sodian hedenbergite, ranging from $Ca_{44}Mg_{29}Fe_{28}$ to $Ca_{37}Mg_{9·0}Fe_{54}$ and with Mg-numbers from 51·0 to 12·5 (calculated with Fe as Fe^{2+}) (Supplementary Data Electronic Appendix 1c). Mg-numbers decrease with increasing host-rock peralkalinity. Oxidation ratios [$Fe^{3+}/(Fe^{3+} + Fe^{2+})$], calculated from stoichiometry, range from 0·01 to 0·22 and are negatively correlated with Mg-number. Sodium contents are also negatively correlated with Mg-number, varying from 0·05 to 0·20 a.p.f.u. All clinopyroxenes are peralkaline, in the sense of having Na/Al >1. Zonation

within crystals is usually limited (En_4), but in one crystal in 150541 En ranges from 12·8 to 21·7%. Clinopyroxene–melt exchange coefficients $Kd^{Fe–Mg}$ (calculated with all Fe as Fe^{2+}) range from 0·11 to 0·13. This is comparable with values (0·14–0·16) found experimentally in a Pantescan pantellerite by Di Carlo *et al.* (2010) and in Kenyan comendites by Scaillet & Macdonald (2003).

Aenigmatite

With increasing host-glass peralkalinity, the aenigmatite phenocrysts in the Green Tuff contain more Na and less Ca and Al (see Mahood & Stimac, 1990) (Supplementary Data Electronic Appendix 2a). The compositional variation can generally be expressed by the coupled substitution $Si^{4+} + Na^{+} \leftrightarrow Al^{3+} + Ca^{2+}$ (Kunzmann, 1999) (Fig. 5). The new analyses extend slightly the compositional range on Pantelleria.

Ilmenite

Ilmenite phenocrysts are in the narrow range X_{ilm} 0·95–0·99, with Nb_2O_5 levels $\leq$0·60 wt % and MnO 1·96–3·19 wt % (Supplementary Data Electronic Appendix 2b).

Magnetite

Limited data are available for magnetite (Supplementary Data Electronic Appendix 2b). The phase rimming an ilmenite phenocryst in 150513 has the composition X_{usp} 0·47–0·49, the core of a microphenocryst in 150541 is X_{usp} 0·62 and an inclusion in olivine is X_{usp} 0·72–0·76.

Apatite

Mahood & Stimac (1990) reported analyses of fluorapatite in three Green Tuff rocks spanning the compositional range trachyte to pantellerite. They noted that the REE and Si contents and the La/Ce and La/Y ratios increased, and Ca and P contents decreased, with increasing host-rock peralkalinity. Our new data (Supplementary Data Electronic Appendix 2c) largely confirm their observations, although slightly increasing the britholite component, as measured by REE + Y + Si contents, up to nearly 5%.

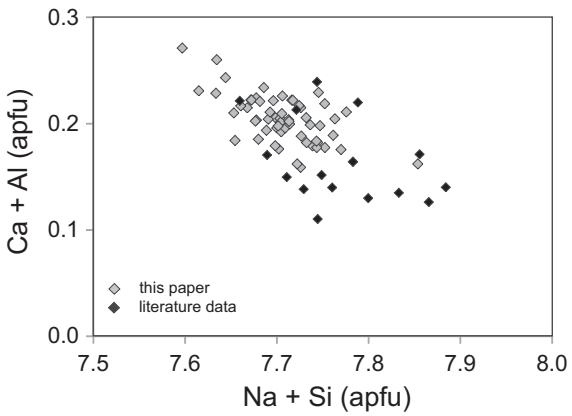

Fig. 5. (Si + Na) plotted against (Al + Ca) for aenigmatite phenocrysts in the Green Tuff. New data from this study, Supplementary Data Electronic Appendix 2a; literature data from Mahood & Stimac (1990), White *et al.* (2009) and Neave *et al.* (2012).

GEOCHEMISTRY

Whole-rock compositions

Compositional modification of peralkaline silicic rocks through secondary hydration and/or partial devitrification is well established (e.g. Noble, 1967, 1970; Noble *et al.*, 1967; Baker & Henage, 1977; Weaver *et al.*, 1990). Particularly important is the potential loss of Na, which affects the calculation of the PI. As an alternative measure of peralkalinity, White *et al.* (2003) introduced the index FK/A [molar (Fe + K)/Al, with all Fe calculated as Fe^{2+}], on the basis that Fe, K and Al are considerably less mobile in aqueous systems than Na and because of the strong positive correlation between PI and FK/Al in non-hydrated peralkaline rocks. A plot of FK/Al against PI for Green Tuff glasses shows a good positive correlation (Fig. 6). However, some point analyses appear to have Na_2O contents rather lower than those predicted from the FK/Al values. Loss of Na cannot, therefore, be precluded from all our samples, especially those with high loss on ignition (LOI) values; for example, 150542 in Table 2, where secondary hydration was the alteration process. Evidence for the loss of Na in a vapour phase is the presence in 160541 of the rare mineral tuhualite ($NaFe^{3+}Fe^{2+}Si_6O_{15}$), which Bagiński *et al.* (2018) showed was precipitated in vesicles during and after devitrification of the tuff. Furthermore, we cannot preclude some loss of Na under the electron beam, which would be more marked in hydrated glasses.

Classification of the whole-rocks has been made using the scheme for peralkaline silicic rocks of Macdonald (1974). In the latter, the data form a continuous trend from comenditic trachyte to pantellerite (Fig. 7). Whole-rock compositions are plotted against SiO_2 in Fig. 8. With increasing SiO_2, the Al_2O_3, TiO_2, MgO and CaO contents decrease and Na_2O and F contents increase; K_2O peaks at SiO_2 ~69 wt % (Fig. 8a). Total Fe decreases to SiO_2 ~66 wt % and then increases.

Barium, Sr (and Ni, Sc and V) contents are negatively correlated with SiO_2; that is, they are enriched in the trachytic members (Fig. 8b). The incompatible trace elements (ITE; Be, Cs, Hf, Nb, Rb, Ta, Th, U and Zr) generally show positive correlations with SiO_2 and PI. Gallium shows an initial increase and then the trend flattens. An important observation is that data from the Montagna Grande Trachyte overlap with those of the Green Tuff, consistent with a genetic relationship between them (Mahood & Hildreth, 1986).

Chondrite-normalized REE patterns for Green Tuff whole-rocks are shown in Fig. 9a. The patterns are light REE (LREE)-enriched; more trachytic types show gently decreasing values from Gd to Lu, whereas the most peralkaline types have flat patterns between Gd and Lu. Europium anomalies (Eu/Eu*) range from 1·08 in

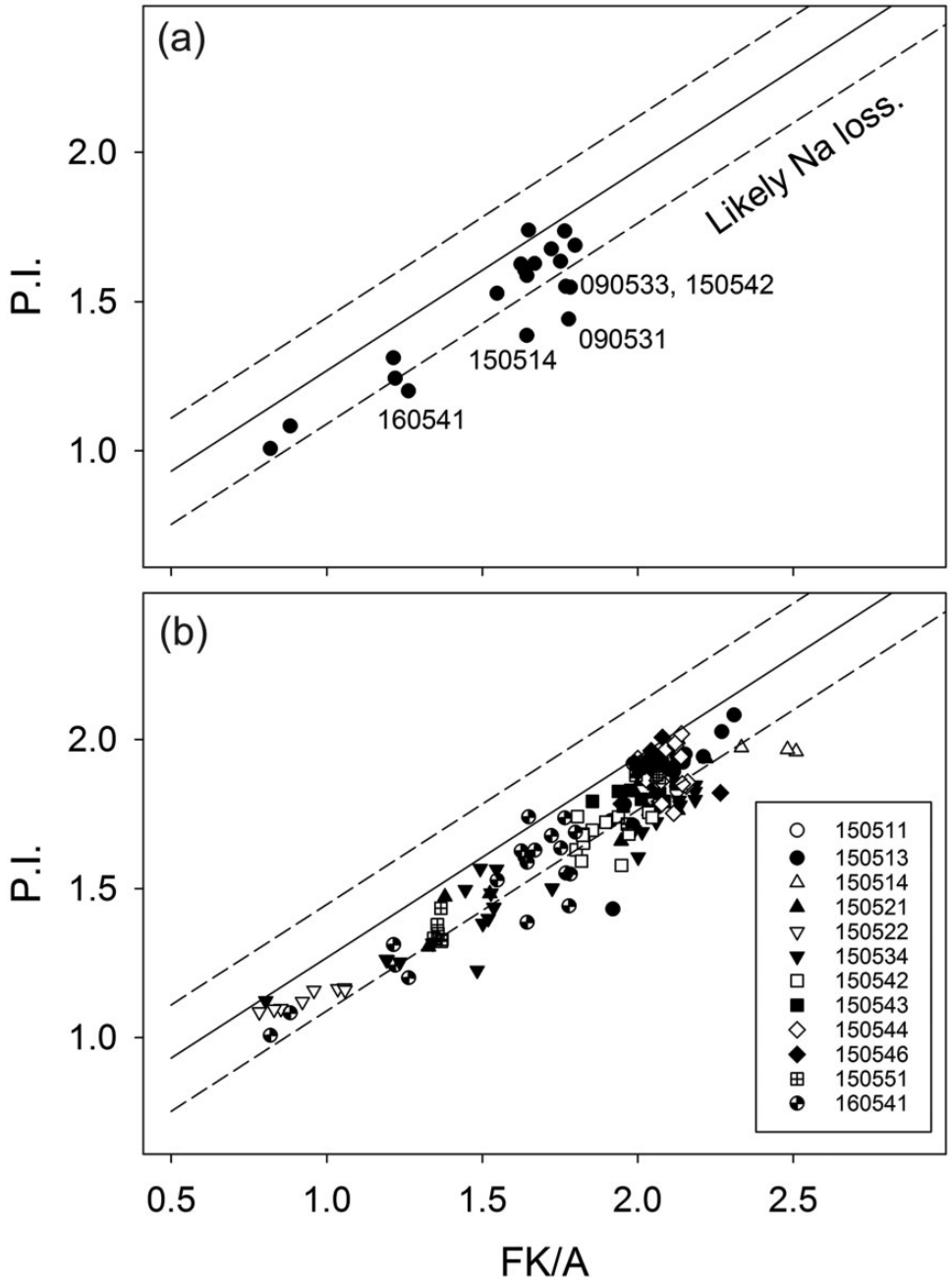

Fig. 6. Plots of the FK/A index [mol (FeO* + K_2O)/Al_2O_3] versus the peralkalinity index [PI = molar (Na_2O + K_2O)/Al_2O_3] to test for potential sodium loss in peralkaline rocks (White *et al.*, 2003). (a) Whole-rock compositions, with potentially altered samples labelled. Data from Table 2. (b) Glass analyses in individual samples (listed). Data from Supplementary Data Electronic Appendix 3.

comenditic trachyte 150522 to 0·41 in pantellerite 160541.

Glass compositions

Representative matrix glass compositions are given in Table 3 and the full dataset in Supplementary Data Electronic Appendix 3. The spread in SiO_2 contents is from 62·8 to 73·7 wt % and the glasses range from comenditic trachyte to pantellerite (Fig. 7). Melt inclusions in phenocrysts cover a similar compositional range (Supplementary Data Electronic Appendix 3) and will be discussed in conjunction with the matrix glass.

As noted above, alkali migration on devitrification and secondary hydration has affected the melt PI, but it appears that the glasses, including the trachytic varieties, were all peralkaline. The compositional variations are generally similar to those in the whole-rocks, although the range extends to both more silica-rich and less silica-rich types (Fig. 8a). It may also be noted that the highest Zr abundance (3183 ppm in sample 150544; Supplementary Data Electronic Appendix 3) is distinctly higher than the maximum recorded in previous studies of Pantescan rocks and glass (2300 ppm; Williams *et al.*, 2014).

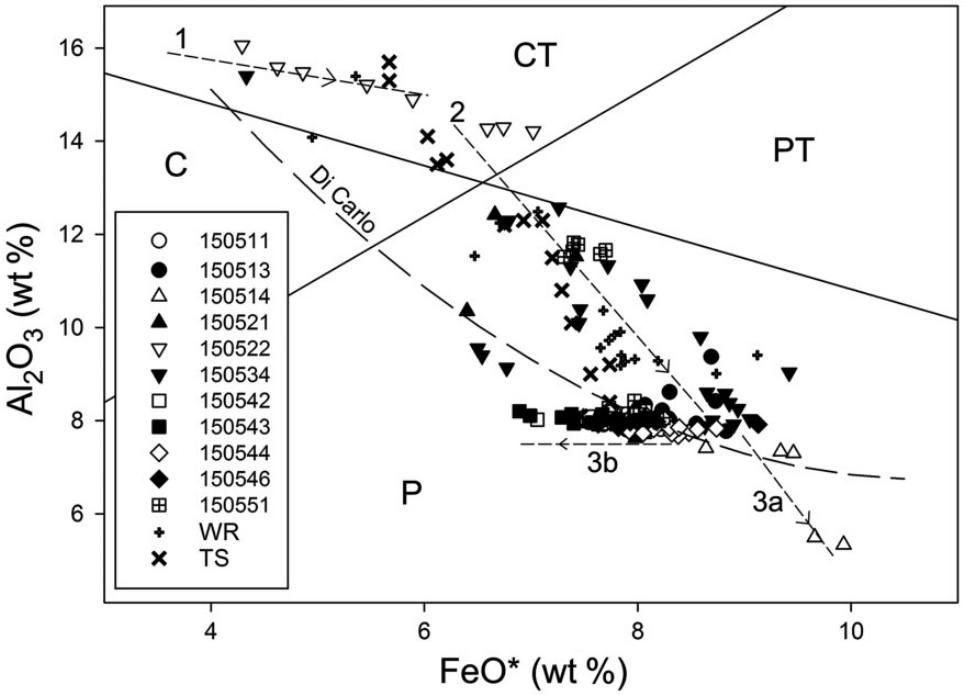

Fig. 7. Whole-rocks (WR) and glass (all symbols except + and ×) for Green Tuff plotted in the classification scheme for peralkaline silicic rocks of Macdonald (1974). CT, comenditic trachyte; C, comendite; PT, pantelleritic trachyte; P, pantellerite. TS, analyses for whole-rocks from the type section of the Green Tuff from Williams *et al.* (2014). Trends 1–3 reflect changing fractionating assemblages (see text for details). The trend marked Di Carlo is for experimental glasses in the study of a Pantescan pantellerite by Di Carlo *et al.* (2010). Data sources: whole-rocks (WR) from Table 2, this study, Mahood & Stimac (1990) and White *et al.* (2009); glass from this study, Supplementary Data Electronic Appendix 3, Mahood & Stimac (1990; samples 7226 and 231/233) and Neave *et al.* (2012; sample 09PNL033).

On a FeO*–Al_2O_3 plot (Fig. 7), the glasses show significantly more complexity than the whole-rocks. The subhorizontal trend across the comenditic trachyte field (Trend 1) shown by samples 150522 and 150534 may be the result of alkali feldspar being the sole liquidus phase in these melts, which results in an increase in FeO*. The change in slope at ~6 wt % FeO* (Trend 2) could mark the onset of clinopyroxene fractionation, after which the glass analyses follow a trend similar to the whole-rock analyses. At ~9 wt % FeO*, two sub-trends emerge. Most glass analyses decrease sharply to ~7 wt % FeO* at near-constant (~7–8 wt %) Al_2O_3 (Trend 3B). The glasses and melt inclusions at ~9 wt % FeO* have a normative composition very similar to the experimentally determined minimum of Carmichael & MacKenzie (1963); we posit that this trend reflects crystallization of aenigmatite along the quartz–feldspar cotectic, which would allow Zr, which is incompatible in all phases (Mahood & Stimac, 1990; Neave *et al.*, 2012), to continue to increase as FeO* decreases and PI remains relatively constant (1·83 ± 0·18 for Zr >1500 ppm).

The other trend (Trend 3A) consists solely of glass and melt inclusions in sample 150514, which continue the whole-rock trend to ~10 wt % FeO* and 5·3 wt % Al_2O_3 (corresponding to PI = 2·61 and 2961 ppm Zr) (Table 3 and Supplementary Data Electronic Appendix 3). These unusually low Al_2O_3 contents, high FeO* contents and high PI make them the most evolved melts yet recorded from Pantelleria (Fig. 7). They are, however, broadly similar to glasses (FeO* 14–15 wt % and Al_2O_3 5–6 wt %) formed in the experiments of Di Carlo *et al.* (2010) and they approach the effective minimum composition for peralkaline silicic magmas (FeO* ~13 wt %, Al_2O_3 ~5 wt %) proposed by Macdonald *et al.* (2012). It is possible that pockets of highly differentiated melt were locally developed in the Green Tuff reservoir, perhaps promoted by the unusually high F contents of the magma, as recorded in the glass in 150514 (≤0·9 wt %; Supplementary Data Electronic Appendix 3). The high F contents could have lowered melt viscosity and allowed crystal fractionation to continue to slightly lower temperatures.

No new REE data for glass are presented here. However, chondrite-normalized REE patterns reported by Mahood & Stimac (1990), Neave *et al.* (2012) and Williams *et al.* (2014). are broadly similar to those of the whole-rocks (Fig. 9b). An unusual feature of several trachytic glass and melt inclusion analyses reported in the literature is positive Eu anomalies (Eu/Eu* = 1·12–1·36), accompanied by Ba concentrations up to 1308 ppm (Mahood & Stimac, 1990; Williams *et al.*, 2014; Romano *et al.*, 2018). Positive Eu anomalies are characteristic of Pantescan basalts that may be parental to these trachytes (Civetta *et al.*, 1998; White *et al.*, 2009). Coupled with low plagioclase/melt partition coefficients for Eu in the basalts (0·13; Neave *et al.*, 2012), it

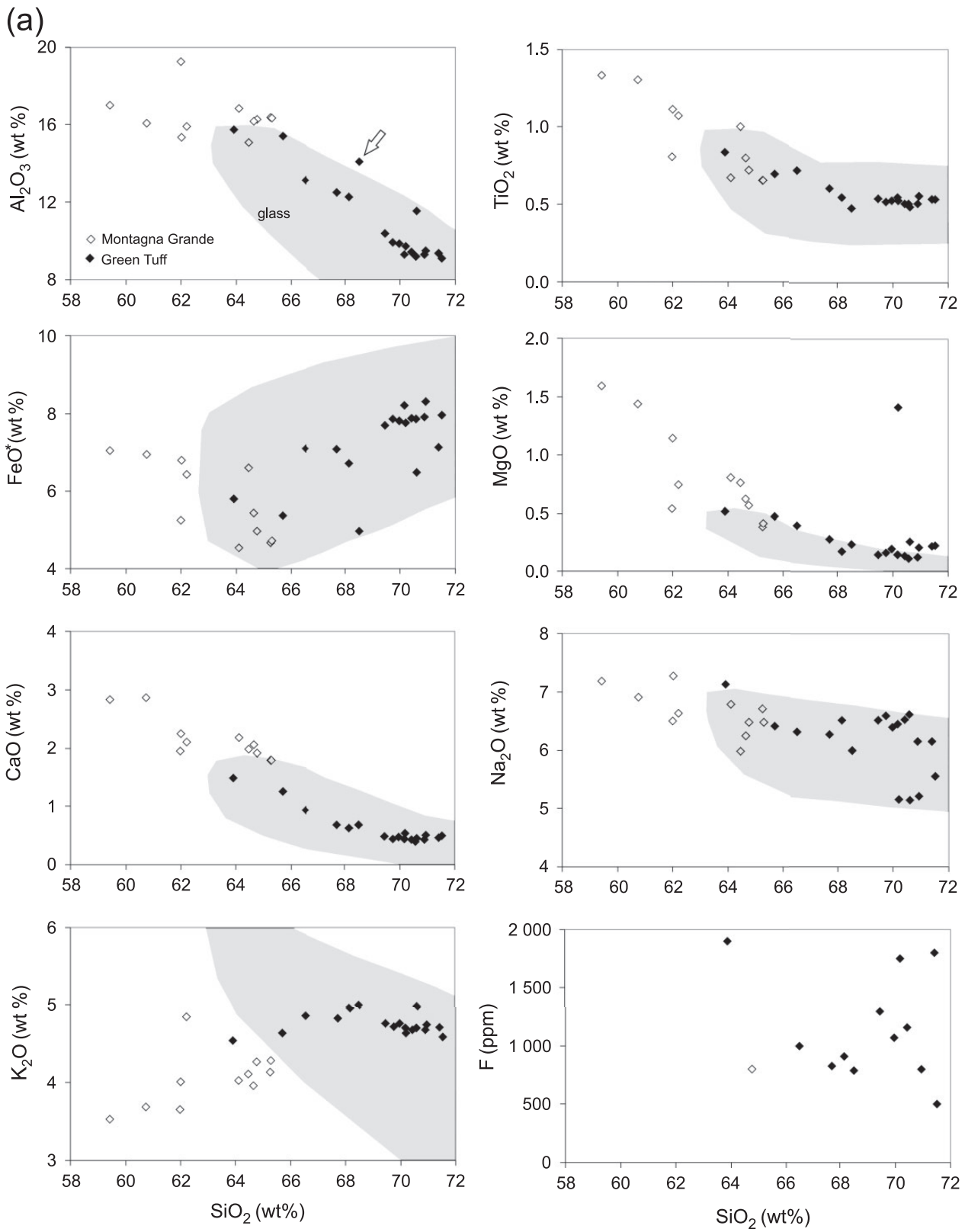

Fig. 8. (a) Selected major element vs SiO_2 plots for Green Tuff whole-rocks. The ranges of glass analyses are shown as fields. (b) Selected trace element vs SiO_2 plots. Data from this study, Table 2, Supplementary Data Electronic Appendix 3, and White *et al.* (2009, samples 060537 and 060545). The arrowed sample (150541) in the Al_2O_3 and Ba plots is thought to be slightly feldspar-accumulitic. Also shown in both plots are whole-rock analyses of trachytes from Montagna Grande and Monte Gibele [data from Villari (1974), Mahood & Hildreth (1986), Avanzinelli *et al.* (2004), Ferla & Meli (2006) and White *et al.* (2009)]. The field for MgO in glass has been drawn omitting two anomalously high analyses.

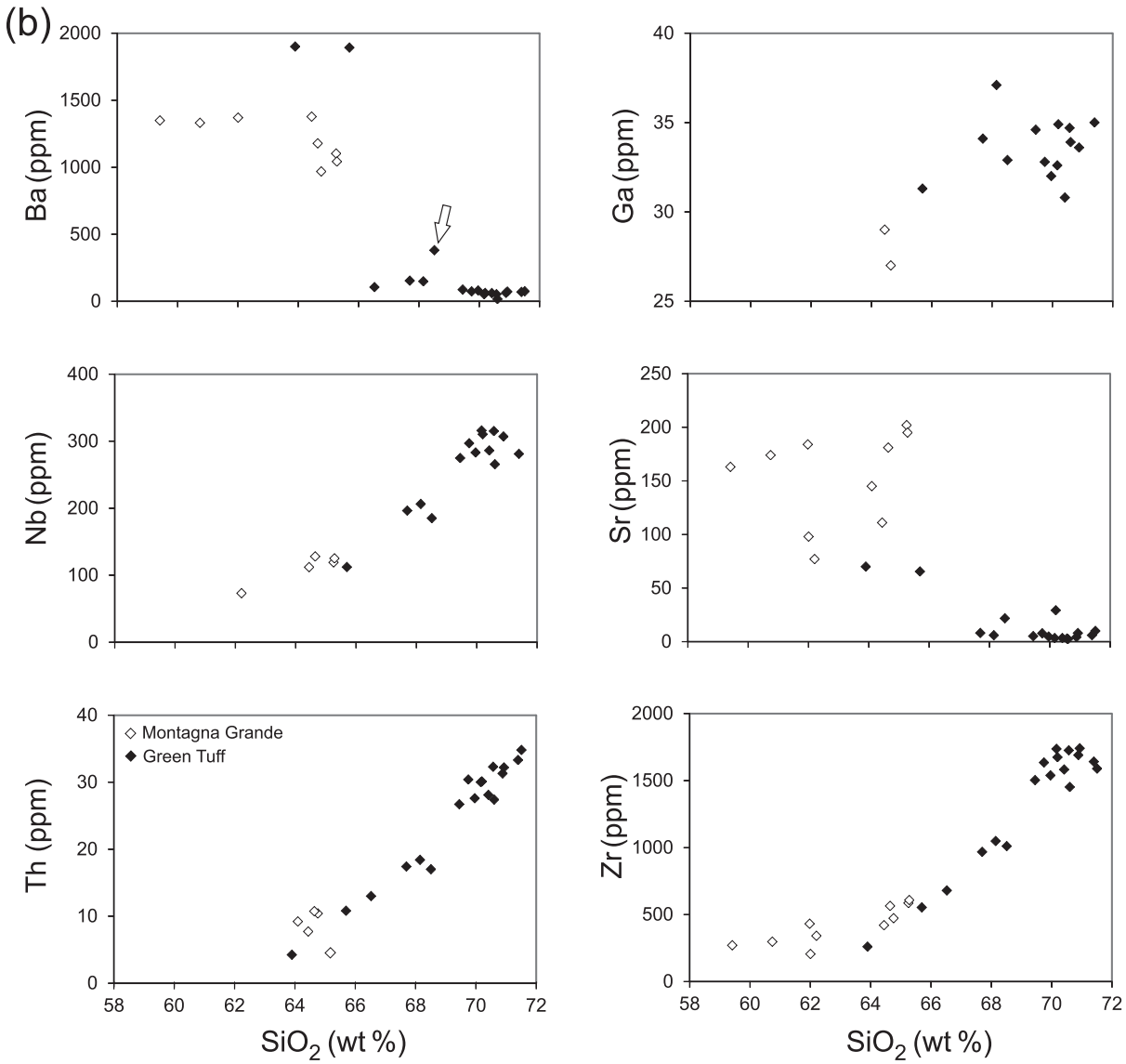

Fig. 8. Continued

is possible that this is an inherited feature preserved through fractional crystallization (Romano *et al.*, 2018). However, crystal accumulation and resorption have also been suggested as differentiation mechanisms for the trachytes (White *et al.*, 2009) and there is petrographic evidence for such a process in our samples, such as modal alkali feldspar abundances up to 40% (Fig. 3a and b). Values higher than ~1300 ppm Ba and Eu/Eu* ≈ 1·36 have been observed only in whole-rock trachyte analyses, strongly suggesting that those samples have been affected by such processes.

This raises the question of the composition of the least evolved trachytic melt in the Green Tuff. This is important because it helps to define the liquid-line-of-descent from intermediate to salic compositions. Williams *et al.* (2014) presented LA-ICP-MS analyses of trachytic glass with 59·90 wt % SiO_2 and 251 ppm Zr. All analyses in their dataset with positive Eu anomalies have about the same SiO_2 and Zr contents. That may well represent, therefore, the trachytic melt parental to the comenditic trachytes.

Chlorine values range continuously from below detection (~250 ppm) in some trachytic glasses to 1·2 wt % (with an outlier at 1·73 wt %) in the pantellerites. Abundances are positively correlated with SiO_2 and Zr, indicating progressive enrichment with increased fractionation. Civetta *et al.* (1988), Lowenstern (1994), Gioncada & Landi (2010) and Lanzo *et al.* (2013) noted that Cl abundances increase more quickly than Zr in glass in various Pantescan suites, suggesting an upward enrichment mechanism in the reservoir. They also suggested that the fact that Cl contents reached ~1 wt % and then remained constant during further magma evolution, as measured by increases in SiO_2

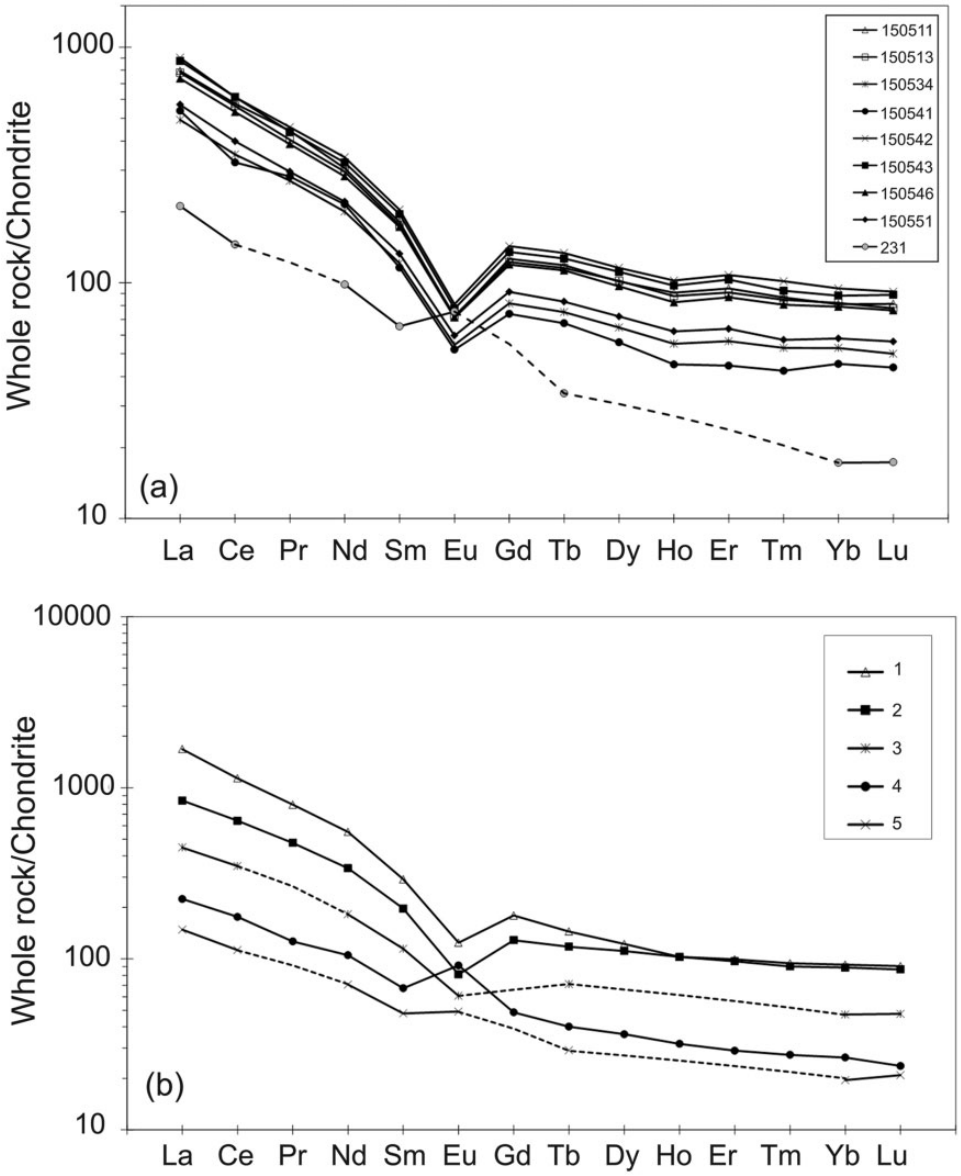

Fig. 9. Chondrite-normalized REE plots for (a) whole-rocks and (b) glasses. Normalizing factors from Sun & McDonough (1989). Data sources: whole-rocks, this study, Table 2, and Mahood & Stimac (1990, sample 231); glass, patterns 3 and 5, Mahood & Stimac (1990; samples 226 and 231), pattern 2, Neave *et al.* (2012; sample 09PNL033) and patterns 1 and 4, Williams *et al.* (2014; samples 44E and 44H). Glass patterns 4 and 5 are comenditic trachyte; patterns 1, 2 and 3 are pantelleritic.

and Zr, pointed to separation of a Cl-bearing fluid phase with which the magmas remained in equilibrium. The new Green Tuff data apparently show a continuing increase of Cl with fractionation, suggesting that Cl remained in the melt phase.

Sulphur abundances (as SO_3) range from below detection (~0·03 wt %) to 0·21 wt %, although the great majority of analyses are <0·1 wt %. These values agree with values for Pantescan rocks given by Civetta *et al.* (1988), Lowenstern (1994), Gioncada & Landi (2010), Neave *et al.* (2012) and Lanzo *et al.* (2013). Abundances show a positive, but scattered, correlation with increasing peralkalinity; it is not clear whether the scatter is due to loss of S on devitrification or to variable loss of a magmatic volatile phase.

An important feature of the glass analyses is the range of compositions within individual samples, shown by SiO_2 and Zr ranges in Table 1, denoting the mingling in varying combinations of trachytic and rhyolitic melts. The range within samples varies from 2 to 9 wt % SiO_2 and its size is not related to the whole-rock composition. Two examples of the mixing components are shown in Fig. 10. In Fig. 10a, a fragment of pale glass with a SiO_2 content of 72–73 wt % contains irregular dark blebs with lower SiO_2 contents (65–68 wt %). The photograph of a thin section of 150521 (Fig. 10b) shows textural intermingling of darker and lighter glass components with SiO_2 values varying from ~67 to 71 wt %. Texturally different glasses in the same specimen do not always show such significant compositional

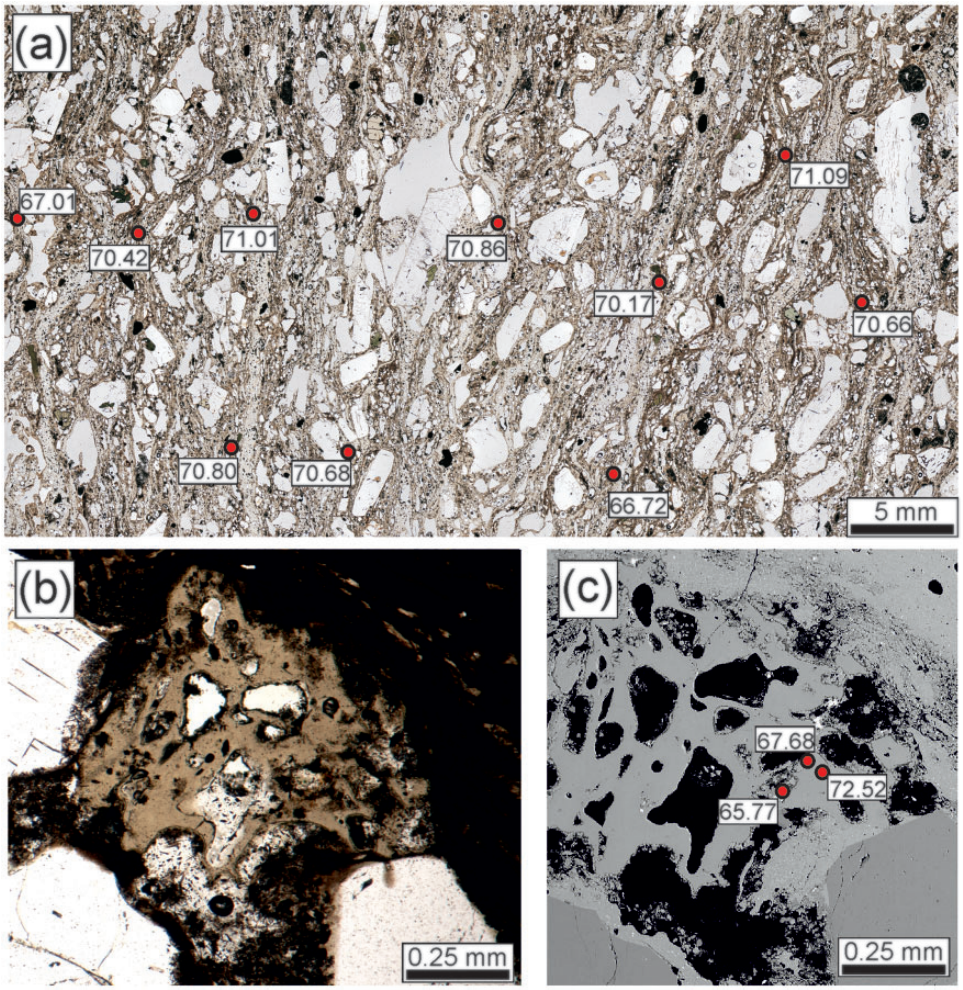

Fig. 10. Examples of different styles of magma mixing in the Green Tuff. Values are for SiO_2 wt %. (a) Streaky intermingling of glass ranging in composition from ~67 to 71 wt % SiO_2. Sample 150551. (b) Fragment of pale brown glass in very dark brown host. Sample 150521. (c) The composition of the pale glass in (b) ranges from 66 to 73 wt % SiO_2.

differences. For example, the pale and dark glasses shown in Fig. 4a have SiO_2 in the ranges 68·7–70·3 and 67·9–70·1 wt %, respectively.

GEOCHEMICAL MODELS

Major element mass-balance models were developed to test the fractional and equilibrium crystallization hypotheses for the origin of compositional zoning and to constrain the relative proportion of the phases involved (Table 4). All calculations were made using Microsoft Office Excel 2013 and are considered acceptable if $\Sigma r^2 < 1{\cdot}0$. The first model (A) tests the origin of highly evolved pantellerite glass from comenditic trachyte matrix glass. The most primitive comenditic trachyte glass analyzed in this study was recovered from sample 150522, and has the lowest Pl (1·09) and FeO* (4·3 wt %) and highest Al_2O_3 (16·1 wt %) observed; this was chosen as the model parent for A. Zirconium concentrations were below the detection limit of the electron probe for this sample. The model daughter selected is an evolved matrix glass at the intersection of two sub-trends recovered from sample 150514 with Pl = 1·96, 9·5 wt % FeO*, 7·3 wt % Al_2O_3 and 2591 ppm Zr.

A second, similar model (B) tests the origin of highly evolved pantellerite melt inclusions hosted in alkali feldspar from sample 150514 with a Pl = 2·61, 10 wt % FeO*, 5·3 wt % Al_2O_3 and 2961 ppm Zr. Both models use a mineral assemblage from sample 150511, which has a composition intermediate between the model parent and daughter. Model results are both acceptable (Σr^2 = 0·255 and 0·240, respectively) and very similar, suggesting that these highly evolved melts can be produced by 93–94% fractional crystallization of an assemblage dominated by alkali feldspar (92·5%) with subordinate clinopyroxene and olivine (2·5–3% each), ilmenite (~1·5%), and apatite (<1%). This model is largely in agreement with previous models of fractional crystallization of the peralkaline trachyte–pantellerite suite at Pantelleria, but also presents the highest estimate for degree of fractional crystallization. The model of White *et al.* (2009), for example, suggested 70% fractional crystallization, but from a more peralkaline parent (Pl = 1·12, 7·0% FeO*) to a less peralkaline daughter (Pl =

Table 4: Results of major element mass-balance modelling**

	Parent	Daughter	Mineral phases					Calc	*r*	Results		
	150522	150514	Anr	Aug	Ol	Ilm	Ap					
Model A, comenditic trachyte glass to pantellerite glass												
SiO_2	65·07	71·38	67·45	49·07	30·37	0·00	0·00	65·08	–0·01	150514	0·07	= *F* (%)
TiO_2	0·71	0·36	0·00	0·21	0·00	52·08	0·00	0·72	–0·01	Anr	0·86	92·5
Al_2O_3	16·05	7·34	18·17	0·44	0·00	0·00	0·00	16·10	–0·04	Aug	0·03	2·8
FeO*	4·30	9·49	0·76	25·20	60·08	45·73	0·57	4·29	0·01	Ol	0·03	3·0
MnO	0·17	0·82	0·00	1·46	4·03	1·99	0·20	0·24	–0·07	Ilm	0·01	1·4
MgO	0·21	0·13	0·00	3·88	4·93	0·20	0·06	0·25	–0·04	Ap	0·00	0·3
CaO	0·76	0·20	0·07	18·79	0·58	0·00	57·13	0·73	0·03		1·00	
Na_2O	6·67	5·90	7·49	0·94	0·00	0·00	0·00	6·86	–0·19			
K_2O	5·97	4·37	6·07	0·00	0·00	0·00	0·00	5·51	0·46			
P_2O_5	0·07	0·00	0·00	0·00	0·00	0·00	42·04	0·11	–0·04			
PI	1·08	1·96						99·90	0·255	$= \Sigma r^2$		
Model B, comenditic trachyte glass to pantellerite melt inclusion												
SiO_2	65·07	72·94	67·45	49·07	30·37	0·00	0·00	65·09	–0·01	Anr	0·87	92·5
TiO_2	0·71	0·73	0·00	0·21	0·00	52·08	0·00	0·72	–0·01	Aug	0·02	2·6
Al_2O_3	16·05	5·34	18·17	0·44	0·00	0·00	0·00	16·08	–0·03	Ol	0·03	3·2
FeO*	4·30	9·99	0·76	25·20	60·08	45·73	0·57	4·29	0·01	Ilm	0·01	1·4
MnO	0·17	0·45	0·00	1·46	4·03	1·99	0·20	0·21	–0·04	Ap	0·00	0·3
MgO	0·21	0·13	0·00	3·88	4·93	0·20	0·06	0·25	–0·04		1·00	
CaO	0·76	0·46	0·07	18·79	0·58	0·00	57·13	0·73	0·04			
Na_2O	6·67	5·63	7·49	0·94	0·00	0·00	0·00	6·86	–0·19			
K_2O	5·97	4·32	6·07	0·00	0·00	0·00	0·00	5·53	0·44			
P_2O_5	0·07	0·00	0·00	0·00	0·00	0·00	42·04	0·12	–0·05			
PI	1·08	2·61					Sum:	99·88	0·240	$= \Sigma r^2$		
Model C, pantellerite glass to pantellerite glass (horizontal trend)												
SiO_2	71·38	71·90	67·25	49·66	40·35	100·00		71·38	0·00	150544	0·92	= *F* (%)
TiO_2	0·36	0·50	0·00	0·39	8·83	0·00		0·81	–0·45	Anr	0·01	6·5
Al_2O_3	7·34	7·73	17·89	0·12	0·50	0·00		7·23	0·11	Cpx	0·01	10·9
FeO*	9·49	8·15	1·09	26·32	40·56	0·00		9·35	0·15	Aen	0·04	48·3
MnO	0·82	0·31	0·00	1·50	1·39	0·00		0·36	0·47	Qtz	0·03	34·3
MgO	0·13	0·09	0·00	3·09	1·09	0·00		0·15	–0·02		1·00	
CaO	0·20	0·26	0·00	17·05	0·55	0·00		0·42	–0·21			
Na_2O	5·90	6·46	7·52	1·87	6·69	0·00		6·27	–0·37			
K_2O	4·37	4·59	6·26	0·00	0·02	0·00		4·26	0·11			
P_2O_5	0·00	0·00	0·00	0·00	0·00	0·00		0·00	0·00			
PI	1·96	2·02					Sum:	100·23	0·654	$= \Sigma r^2$		

Minerals: Anr, Anorthoclase; Cpx, clinopyroxene; Ol, olivine; Ilm, ilmenite; Ap, apatite; Aen, aenigmatite; Qtz, quartz. Model results: *F*, liquid proportion; Σr^2, sum of the squares of the residuals. Apatite and aenigmatite compositions adapted from White *et al.* (2009). PI, Peralkalinity Index [molar $(Na_2O + K_2O)/Al_2O_3$].

1·91, 7·8% FeO*). However, this and other models (e.g. Civetta *et al.*, 1998; Neave *et al.*, 2012) all agree on a dominant role for alkali feldspar (>85% of the fractionating assemblage), with subordinate olivine, clinopyroxene, Fe–Ti oxides and apatite, consistent with the observed mineral assemblages in these samples. Although we lack Zr data for the comenditic trachyte glass, Williams *et al.* (2014) reported an average value of 255 ppm for one glass sample within the comenditic trachyte facies of the Green Tuff type section; if we assume bulk $D_{Zr} \approx 0$, then $F = 0{\cdot}09$–$0{\cdot}10$ (91–90% crystallization), which is consistent with our results.

A curious feature observed in Fig. 7 is a subhorizontal trend at ~7·5 wt % Al_2O_3 that extends from the end of the main trend (model A) to progressively lower concentrations of FeO* that nonetheless include glasses with the highest concentrations of Zr measured (up to 3108 ppm), despite near-uniform Zr whole-rock concentrations (1500–1700 ppm). This trend is also manifest in Figs 11 and 12b (see below), where these samples appear to plot along the experimental alkali feldspar–quartz cotectic (Carmichael & MacKenzie, 1963). These highly evolved samples have assemblages characterized by a relatively large volume of aenigmatite (e.g. 2–3% in 150514), along with quartz, alkali feldspar and clinopyroxene; we suggest that this trend is the result of equilibrium crystallization of this assemblage. Mass-balance modelling of this scheme (Table 4, Model C) suggests its plausibility ($\Sigma r^2 = 0{\cdot}655$, with 0·221 error from MnO), with a small degree (8%) of late crystallization of an assemblage of aenigmatite and quartz with minor quantities of alkali feldspar and sodian clinopyroxene, resulting in a decrease in FeO* with a slight rise in Al_2O_3 and PI. An estimate of the degree of crystallization from Zr ratios (assuming $D_{Zr} \approx 0$, as above) between the model daughter and parent suggest about twice as much crystallization (17%, $F = 0{\cdot}83$) as that determined by major element mass-balance modelling.

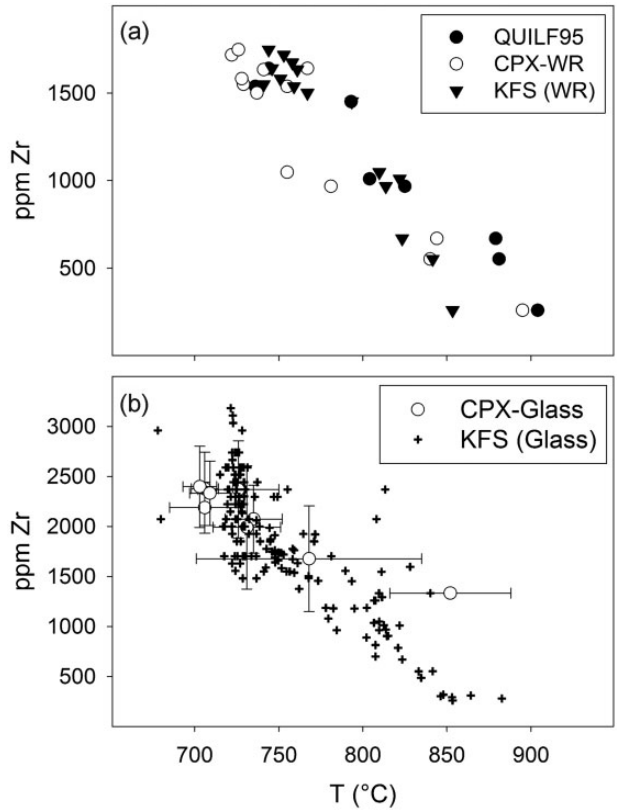

Fig. 11. (a) Comparison of calculated temperatures (°C) for whole-rock compositions and assemblages plotted against Zr concentration. QUILF95 points are calculated from olivine–clinopyroxene equilibria (Andersen *et al.*, 1993). CPX-WR are calculated from clinopyroxene–whole-rock compositions (Putirka *et al.*, 2003). KFS were determined from the position of the whole-rock composition in Fig. 12 (see text for details). (b) Comparison of calculated temperatures for glass compositions plotted against Zr concentration, determined with the techniques described in (a). Averages with error bars are plotted for CPX and individual points are plotted for KFS to facilitate readability.

Overall, the results of the modelling are consistent with the various magmas having been formed by fractional crystallization of the observed phenocryst assemblages.

GEOTHERMOMETRY

In Fig. 11, temperatures calculated using (Fig. 11a) QUILF (olivine + clinopyroxene) and (Fig. 11b) by clinopyroxene–glass and clinopyroxene–whole-rock (Putirka *et al.*, 2003) (Table 5) geothermometers are plotted against Zr contents in the whole-rocks. Although the QUILF results give higher temperatures at a given Zr content, it is clear that the least evolved trachytes give ~900°C and the temperatures then decrease to ~700°C in the most peralkaline members. There must, of course, have been local temperature fluctuations owing to mixing of magmas from different layers. Oxygen fugacities range from FMQ –0·5 to FMQ –1·5 (where FMQ is fayalite–magnetite–quartz), with an outlier at FMQ –2·2 (Table 5). The temperature and fO_2 estimates are similar to those for Pantescan pantellerites calculated thermodynamically by White *et al.* (2005, 2009) and determined experimentally by Di Carlo *et al.* (2010). Thermodynamic values recovered by olivine–clinopyroxene equilibria in the QUILF system are pressure-sensitive, but for an increase (or decrease) of 500 bars of pressure, silica activity changes by only 0·02 units and temperature increases (or decreases) by only 3°C on average. However, oxygen fugacity, relative to the FMQ buffer, remains relatively unchanged.

Whole-rock (Fig. 12a) and glass (Fig. 12b) analyses have been plotted in the system Q–Ab–Or–H_2O with 8·3 mol % aegirine + 8·3 mol % sodium metasilicate added, P_{H2O} = 1000 bar, and projected from H_2O + aegirine + sodium metasilicate (Carmichael & MacKenzie, 1963) (Fig. 12). The normative mineralogy was calculated with FeO/FeO* = 0·9, corresponding to oxygen fugacities buffered at FMQ –1 between 700 and 900°C (Sack *et al.*, 1980). The alkali feldspar liquidus surface is plotted as crosses, labelled with the experimentally determined temperature (°C) for that composition. The minimum for this system occurs at $Q_{40·5}Or_{34·5}Ab_{25}$, with the alkali feldspar–quartz cotectic located at approximately Q_{40}. Also shown is the 'thermal valley' of Carmichael & MacKenzie (1963), the differentiation path of a system undergoing crystal fractionation of alkali feldspar with a composition of $\sim Or_{35}$. Despite some scatter, temperatures drop from 825°C in the trachytes to 700°C in the most peralkaline whole-rocks, temperatures consistent with those indicated in Fig. 11, and the rocks generally follow a feldspar fractionation trend. The spread of glass compositions at Or_{40} is consistent with some melts having reached the quartz–feldspar cotectic.

The vertical decrease in temperature from the comenditic trachyte to the pantellerite is accompanied by an increase in silica activity relative to quartz saturation [$aSiO_2$ (Qtz)], calculated by QUILF95, from 0·74 to 1·0, as well as a slight increase in oxygen fugacity relative to the FMQ buffer (Fig. 13). Macdonald *et al.* (2011) described the antipathetic relationship between fayalitic olivine and aenigmatite as a function of T, P and $aSiO_2$, with the latter crystallizing at the expense of the former at $T < 750$°C, at silica activities close to or at quartz saturation at 150 MPa. Lower pressures extend the stability of aenigmatite to higher temperatures (see White *et al.*, 2005; Di Carlo *et al.*, 2010), which is consistent with these results.

Fayalite-bearing rhyolites with ilmenite present as the sole Fe–Ti oxide phase crystallize in T–fO_2 space along the displaced FHQ (fayalite–hematite–quartz) buffer. In this sense, the FHQ buffer is 'displaced' from that which would plot for unit activities for all phases. A regression through the T–$aSiO_2$ data was used to calculate the displaced FHQ buffer for ilmenite compositions between X_{ilm} 0·95 and 0·98 in Fig. 13. In our formulation, unit activity is assumed only for fayalite and the curve is displaced to lower fO_2 owing to much lower hematite activities (X_{hem} = 0·03–0·05; activities

Table 5: Results of geothermometry and oxygen barometry calculated with QUILF95 (Andersen *et al.*, 1993)

		Ilmenite			Spinel			Olivine		Augite					
Sample		X-Hem	X-Gk	X-Py	N-Ti	N-Mg	N-Mn	X-Fo	X-La	X-En	X-Wo	$aSiO_2$(Q)	T(°C)	log fO_2	ΔFMQ
160541	Input	0·042	*0·013*	0·047				0·079	*0·008*	0·125	0·428				
	Calc		0·012						0·008			0·942	793	–15·7	–1·01
150513	Input	0·047	*0·024*	0·056				0·069	0·006	*0·112*	0·435				
	Calc		0·009							0·121		0·976	736	–16·6	–0·58
150522	Input	+						0·251	0·009	*0·283*	0·270				
	Calc									0·270		0·743	881		
150534	Input	0·035	*0·016*	0·044	0·723	*0·017*	0·053			0·101	0·424				
	Calc		0·010	0·032		0·012						0·773	820	–15·8	–1·73
150541	Input	+			0·667	*0·021*	0·055	0·153	0·007	*0·195*	0·419				
	Calc					0·026				0·207		0·904	804	–15·2	–0·78
150551	Input	0·013	*0·008*	0·042				0·126	0·011	*0·138*	0·423				
	Calc		0·021							0·170		0·860	863	–15·4	–2·20
231	Input				0·719	*0·042*	0·057	0·262	0·009	*0·296*	0·410				
	Calc					0·058				0·275		0·816	904	–13·4	–0·95
226	Input				0·763	*0·039*	0·056	0·140	0·010	*0·203*	0·405				
	Calc					0·029				0·181		0·922	879	–14·2	–1·31
060537	Input	0·039	*0·009*	0·050				0·058	0·006	*0·113*	*0·422*	1·000			
	Calc		0·008							0·103	0·427		744	–16·7	–0·89

All results are calculated at $P = 100$ MPa. Entries in italics in the 'Input' row signify values that were set as trial values; the values calculated by QUILF95 are in normal font in the 'Calc' row. Silica activity is relative to quartz saturation. ΔFMQ = log fO_2 – FMQ(T). Samples 231 and 226 are from mineral analyses reported by Mahood & Stimac (1990); sample 060537 is from mineral analyses reported by White *et al.* (2009). +, present but not analyzed.

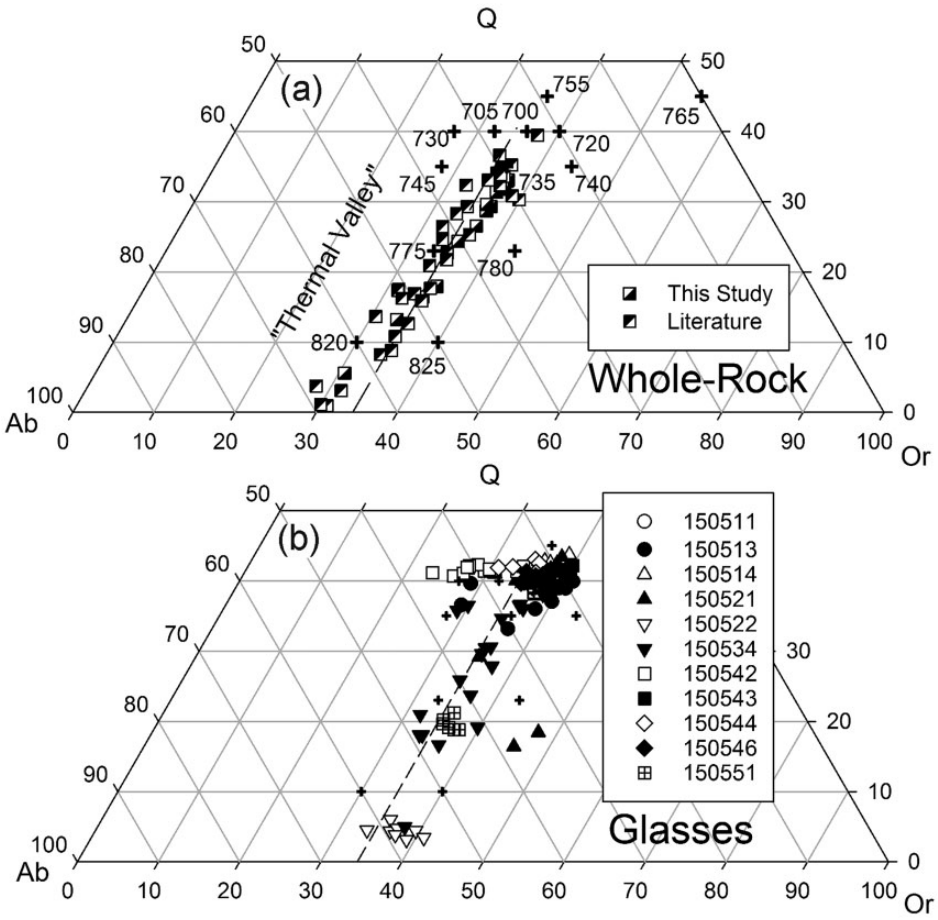

Fig. 12. (a) Whole-rock and (b) glass analyses plotted in the system Q–Ab–Or–H_2O with 8·3 mol % aegirine + 8·3 mol % sodium metasilicate added and $P_{H2O} = 1000$ bar (Carmichael & MacKenzie, 1963). Whole-rock analyses displayed include those from this study (Table 2) and from the literature (Civetta *et al.*, 1984, 1998; Kovalenko *et al.*, 1994; Esperança & Crisci, 1995; Avanzinelli *et al.*, 2004; Ferla & Meli, 2006; White *et al.*, 2009; Williams *et al.*, 2014). The crosses mark the alkali feldspar liquidus surface.

calculated following Andersen & Lindsley, 1988) and silica activities relative to quartz saturation less than unity (interpolated from the linear trend in the previous figure, with silica activities calculated from olivine–clinopyroxene equilibrium using QUILF95).

The Green Tuff broadly follows the FHQ curve, with the magma chamber becoming slightly less reduced roofward relative to the FMQ buffer. A comparison with experimental data from pantelleritic systems, including Eburru, Kenya (Scaillet & Macdonald, 2006) and Pantelleria (Di Carlo *et al.*, 2010), suggests that this may be due to a corresponding volatile gradient from ~1 wt % H_2O in the comenditic trachyte to ~4 wt % H_2O in the pantellerite. The presence of such a volatile gradient may be supported by Fourier transform infrared (FTIR) analyses of melt inclusions in the basal pantellerite and uppermost trachyte. Melt inclusions in the trachyte are comenditic trachyte in composition, with 0·15–1·05 wt % H_2O (Romano *et al.*, 2019). Lanzo *et al.* (2013) reported values of up to 4·2 wt % H_2O from feldspar-hosted melt inclusions in the pantelleritic basal fall unit, consistent with values from melt inclusions in

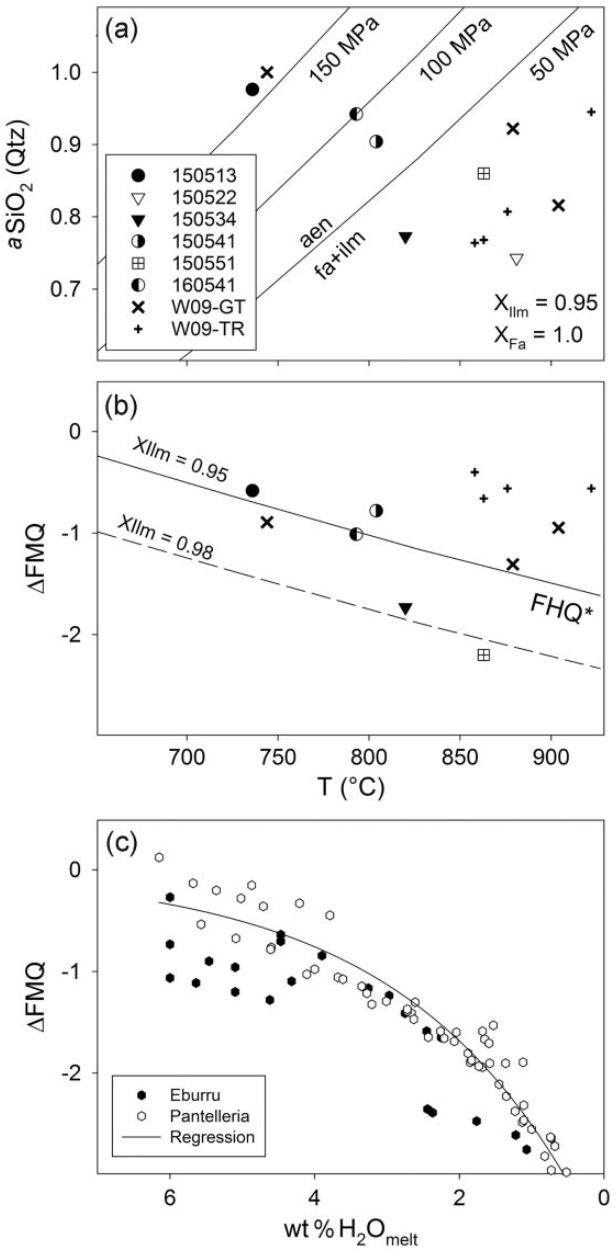

Fig. 13. (a) Silica activity ($aSiO_2$) relative to quartz saturation and (b) oxygen fugacity relative to the FMQ buffer plotted against temperature. W09-GT and W-O9-TR are the results of QUILF95 geothermobarometry for the Green Tuff and Montagna Grande Trachyte, respectively, from White *et al.* (2009). The fayalite–ilmenite–aenigmatite stability curve for $X_{Ilm} = 0.95$ is calculated following Macdonald *et al.* (2011), with ilmenite activities calculated using the solution model of Andersen & Lindsley (1988). ΔFMQ = log fO_2 – FMQ(T), with FMQ(T) calculated following Frost *et al.* (1988). (c) The experimental results of Scaillet & Macdonald (2006) for Eburru and Di Carlo *et al.* (2010) for Pantelleria show the strong positive correlation between oxygen fugacity (as ΔFMQ) and melt water content (wt % H_2O_{melt}).

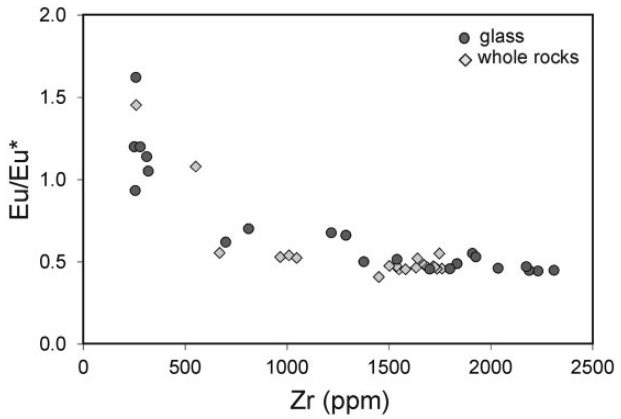

Fig. 14. Eu/Eu* plotted against Zr content for Green Tuff samples. Data sources: whole-rocks from this study, Table 2, Mahood & Stimac (1990) and White *et al.* (2009); glass from Mahood & Stimac (1990, samples 7, 226, 231/233), Neave *et al.* (2012, sample 09PNL033) and Williams *et al.* (2014, samples 44H and 44I).

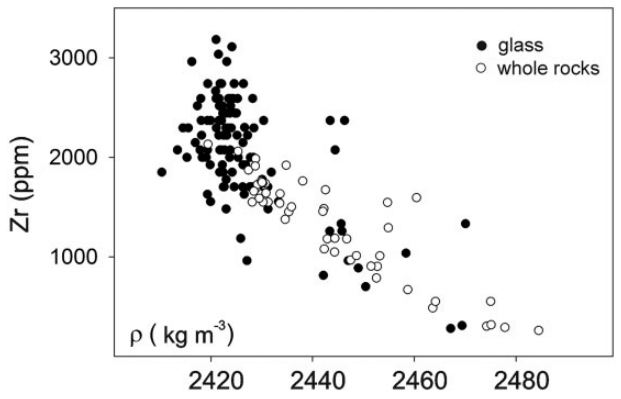

Fig. 15. Anhydrous melt densities, calculated by the method of Bottinga & Weill (1970), plotted against Zr contents for whole-rocks (open circles) and glasses (filled circles). The densities initially decrease to Zr ~1500 ppm and then change little with increasing Zr. Data sources: this study, Table 2 and Supplementary Data Electronic Appendix 3.

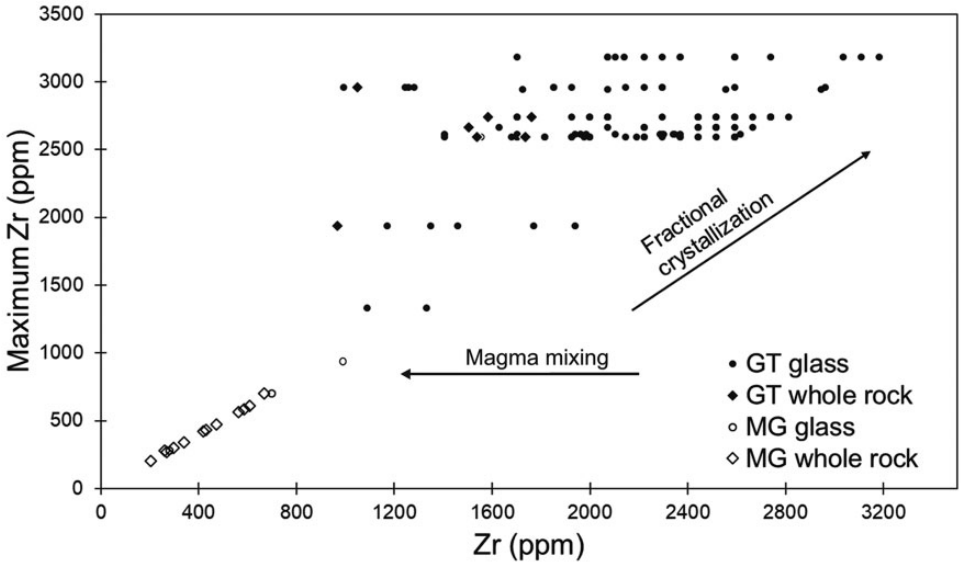

Fig. 16. Maximum Zr content in glass in each Green Tuff whole-rock plotted against range of Zr contents in glass of the same rock. The ranges indicate mixing in varying proportions of trachytic and rhyolitic melts. Also shown is the composition of a Montagna Grande glass, from Mahood & Stimac (1990, sample 119); its relative compositional similarity to the Montagna Grande whole-rocks suggests that the range of glasses in each sample must be small. Montagna Grande whole-rock data from Mahood & Stimac (1990), Avanzinelli *et al.* (2004), Ferla & Meli (2006) and White *et al.* (2009).

compositionally similar pantellerite lavas (up to 4·9 wt % H_2O; Gioncada & Landi, 2010; Neave *et al.*, 2012).

Using the model parameters of White *et al.* (2009), the simplest explanation for a volatile gradient is ~70% fractional crystallization of a comenditic trachyte melt with 1·0–1·5 wt % H_2O, which would produce a pantellerite melt with 3·3–4·9 wt % H_2O (assuming bulk D_{H2O} = 0·01). This in turn would require 0·3–0·5 wt % H_2O in the parental basalts—lower than either the 0·9–1·6 wt % reported by Gioncada & Landi (2010) for melt inclusions in the Cuddie Rosse basalt or the 1·0–1·5 wt % predicted from MELTS modelling (White *et al.*, 2009). The MELTS results reported by White *et al.* (2009) suggest that basalt water concentrations as low as 0·5 wt % would also produce similar comenditic trachyte. The volatile gradient and accompanying change in oxidation state could also be explained by melt vesiculating, which could result in a reaction between Fe-rich silicate melt and H_2O via thermal dissociation and degassing of H_2 (see Carmichael, 1991; Mungall & Martin, 1995; Scaillet & Macdonald, 2001; White *et al.*, 2005).

DISCUSSION

Nature of the Green Tuff magma reservoir

Prior to eruption, the Green Tuff magma reservoir is envisaged with a trachytic crystal mush overlain by a layered pantelleritic upper part of the chamber. Pressure estimates of 100 MPa, which correspond to depths of 3–4 km, were used for all thermodynamic calculations because (1) this is within the total range of 50–150 MPa estimated by previous workers for the depth of the magma chamber using various methods, and (2) this depth is consistent with geophysical studies of the depth of the magma chamber; for example, with the model of Mattia *et al.* (2007), based on geodetic data, placing the top of the reservoir at ~4 km beneath the caldera. The overall depth of the reservoir would have been greater if the Montagna Grande trachytes were part of the magma system; they were erupted from lower layers in the reservoir during resurgence following eruption of the Green Tuff, although the depth of magma being tapped is not known. Major element contents are consistent with such a cogenetic relationship (Figs 7 and 8a) and, although trace element data are rather scarce for Montagna Grande, the trace elements are also consistent; average Zr/Nb ratios, for example, are 4·9 in the Green Tuff and 4·5 in the Montagna Grande trachytes. The speculative gabbroic mush represents the source of the trachytic magmas, squeezed out by either compaction or buoyancy.

Similar models for trachyte–peralkaline rhyolite relationships have been proposed by Troll & Schmincke (2002) for ignimbrite 'A', Gran Canaria, and by Sumner & Wolff (2003) for the 'TL' ignimbrite, Gran Canaria.

Origin of compositional zonation

Previous researchers have used geochemical modelling to show that the transition from trachyte to rhyolite at Pantelleria can be satisfactorily modelled by fractionation of an alkali feldspar–olivine–clinopyroxene–oxide ± aenigmatite assemblage (Civetta *et al.*, 1988; White *et al.*, 2009; Neave *et al.*, 2012). The new models presented here are consistent with these earlier models. Experimental studies of Pantescan rocks by Di Carlo *et al.* (2010) and Romano *et al.* (2018) are also consistent with such models. We propose, therefore, that the comenditic trachytes separated from the crystal-rich

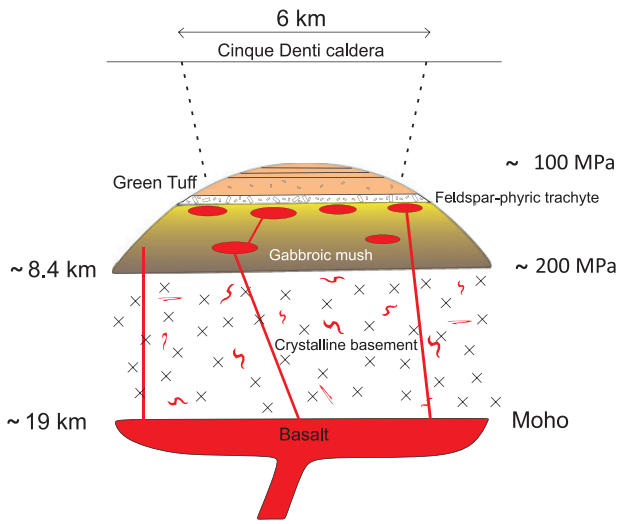

Fig. 17. Possible relationships in the magmatic plumbing system prior to eruption of the Green Tuff. Basaltic magma has ponded both at the base of the crust and below the feldspar-rich trachytic magmas that were erupted as the lowermost portion of the Green Tuff and the Montagna Grande Trachyte. In both settings, the basalt fractionated through towards intermediate compositions. The crustal structure is from Civile *et al.* (1988).

metaluminous trachytes later erupted as the Montagna Grande Trachyte. Continued fractional crystallization of the trachytic magmas generated pantelleritic melts, which separated from the trachytes through buoyancy effects and accumulated towards the roof of the reservoir, finding levels determined by their density.

Some of the compositional variation in the Green Tuff has also been related to alkali feldspar accumulation (Korringa & Noble, 1972; Prosperini *et al.*, 1990; White *et al.*, 2009). For example, the so-called low-incompatible trace element (low-ITE) trachytes of White *et al.* (2009) were shown to contain up to 47% modally of alkali feldspar phenocrysts. The new dataset provides further evidence that the process was important in the evolution of the Green Tuff. For example, at ~300 ppm Zr, the Eu anomaly increases from 1 to 1·6 (Fig. 14). At the same Zr content, K/Rb ratios rise from ~600 to 1000, Ba contents from ~700 to 2300 ppm and Sr contents from ~50 to 70 ppm, features consistent with feldspar accumulation in the trachytic rocks. Major and trace element models presented by White *et al.* (2009) and Romano *et al.* (2018) suggest that samples affected by accumulation or resorption of alkali feldspar will have Ba >1300 ppm. The process was also locally operative at higher levels in the chamber; sample 150541, with ~35 modal % feldspar phenocrysts, has high Al_2O_3, Ba and Sr (Fig. 8) contents. However, it has a negative Eu anomaly (Eu/Eu* 0·54) which would require that the accumulating feldspar had a negative anomaly. Mahood & Stimac (1990) have, nevertheless, argued that all the feldspars in the Green Tuff have strong positive Eu anomalies.

It appears, therefore, that the composition of the comenditic trachyte underlying the pantellerites was modified by variable amounts of feldspar accumulation.

Glass heterogeneity and implications for syneruptive mixing

Density variations in the melts (glasses) have been calculated by the method of Bottinga & Weill (1970) (Fig. 15). Anhydrous densities range from 2480 kg m^{-3} in the trachytes to 2420 kg m^{-3} in the most peralkaline melts. This might imply that the pantelleritic part of the reservoir was stably density-stratified whereas the higher density and viscosity of the feldspar-rich trachytes prevented them from rising and mixing with the overlying rhyolites. This further implies that eruption of the Green Tuff was triggered by an external mechanism. We suggest that the trigger was influx of more mafic magma into the trachytic parts of the reservoir, which raised the temperature (as seen in the resorption of phenocrysts) and caused trachytic melts to rise and mix with the overlying more evolved melts (see Flude *et al.*, 2008; Romengo *et al.*, 2012). Triggering of the eruption of peralkaline magmas by intrusion of intermediate magmas has been proposed by Sumner & Wolff (2003) for ignimbrite 'TL' (Gran Canaria) and by Pimentel *et al.* (2016) for the comenditic trachytes of the AD 1761 eruption at Terceira (Azores). The lack of significant compositional zoning in the resorbed phenocrysts is taken to show that the more mafic magma acted as a heat source without physical or chemical mixing, as discussed by D'Oriano *et al.* (2017) for similar feldspar-rich zones in comenditic trachytes of the Lajes ignimbrite eruption, Terceira, Azores.

Models of magma evacuation from compositionally zoned chambers have shown how each successive evacuation drew magma from progressively deeper levels of the chamber, isochemical surfaces being deflected upwards beneath the vents so that several compositional layers can be tapped simultaneously (Blake, 1981; Blake & Ivey, 1986; Spera *et al.*, 1986; Schuraytz *et al.*, 1989; Macdonald *et al.*, 1994). It was noted earlier that many Green Tuff samples show a range of matrix glass compositions, denoting the mingling in varying combinations of trachytic and rhyolitic melts. Importantly, the mingling was very thorough, down to the micron scale, which we ascribe to the small differences in temperature and density between the pantelleritic melts, which did not significantly hinder mixing.

The range of SiO_2 contents in the glasses is matched by variations in Zr (Table 1). It appears, therefore, that the steady increase in Zr shown with increasing height in the pre-eruptive chamber by Williams *et al.* (2014) does not simply reflect an increasing degree of fractionation of the melt upwards. Rather, it reflects an increasing proportion of evolved melts in earlier erupted magma batches. Plotting the highest Zr content in each sample, as a measure of the sample's highest stratigraphic position within the pre-eruptive chamber, against the range of Zr contents in the same glasses, two broad zones can be distinguished (Fig. 16): (1) a zone where the glasses all have rather homogeneous

(?)trachytic composition; (2) a zone where the glasses are dominantly mixes of trachytic with rhyolitic melts. Two barriers to mixing thus existed in the system: one between crystal-rich and crystal-poorer comenditic trachytes and one between the trachytes and pantellerites.

An important general point arising from the within-sample ranges in glass composition is that whole-rock analyses do not necessarily give a true indication of the range of melt compositions in the pre-eruptive reservoir; as noted above, the highest whole-rock and glass Zr contents are 2300 ppm and 3183 ppm, respectively. This raises the question of how common this type of fine-scale mingling may be in compositionally zoned silicic systems. Clearly, relevant studies would preferably need to be made in systems preserving significant glassy facies. However, in their absence a careful analysis of the stability relationships of the phenocryst assemblages should provide clues to the range of host melts.

Significance for the Daly gap

Models for the formation of the Pantescan suite are broadly divisible into two groups. In one, the trachytes and rhyolites were formed independently of basaltic magma; intermediate compositions (mugearites and benmoreites) are the products of magma mixing (Lowenstern & Mahood, 1991; Avanzinelli *et al.*, 2004; Ferla & Meli, 2006; Romengo *et al.*, 2012). In the other model, the salic rocks were formed by the prolonged crystal fractionation of basaltic magma. The observed scarcity or absence of intermediate rocks results from either a physical or a thermodynamic discrimination in the magma reservoirs and their non-eruption (Civetta *et al.*, 1988; White *et al.*, 2009; Neave *et al.*, 2012). One aim of this study has been to assess whether melts of intermediate composition were present in the Green Tuff magma system. Some of the published evidence is equivocal. Geochemical modelling had shown that the pantellerites of Pantelleria could have been produced by ~95% fractional crystallization of parental alkali basalts, via magmas of intermediate composition. In the modelling of White *et al.* (2009), melts entered the Daly gap after 30% crystallization, and then stayed there for a further 59% crystallization. In contrast, in experiments made on a Pantescan basalt at 1 atm and 8 kbar, Mahood & Baker (1986) found that residual melts had not reached the Daly gap (~50–62 wt % SiO_2) after 70% crystallization.

The main approach used here was to carefully relate glass and mineral compositions to textures. The least evolved glass composition in the new Green Tuff dataset has 62·84 wt % SiO_2; similar glass compositions (SiO_2 59·90–62·3 wt %) have been recorded in the Green Tuff by Mahood & Stimac (1990) and Williams *et al.* (2014). No clearly intermediate-composition melts have thus been found.

As an indicator of what mineral compositions might be expected, in their MELTS modelling of the evolution of Pantescan suites White *et al.* (2009) found the following mineral compositions as melts passed through the benmoreite stage (at 1·0% H_2O in the parent, 100 MPa, FMQ –1): plagioclase $An_{60–49}$; olivine $Fo_{47–21}$; clinopyroxene $Wo_{45}En_{35–30}Fs_{20–25}$. For this study, a careful analysis was made of the cores of phenocrysts in the Green Tuff, on the basis that they may have preserved compositions from earlier stages of magma evolution. For feldspar, the most 'mafic' composition was $An_{7·9}$; for olivine $Fo_{25·4}$; for clinopyroxene En_{29}. The main phenocryst phases thus crystallized from melts more evolved than benmoreite.

White *et al.* (2009) described, from the post-caldera trachyte lavas of Montagna Grande and Monte Gibele, anorthoclase phenocrysts ($An_{3–9}Ab_{70–71}Or_{20–26}$) with cores of resorbed plagioclase ($An_{34}Ab_{62}Or_4$). A benmoreitic lava from Montagna Grande, thought to have formed by mixing of trachytic and mafic magmas, contains feldspar phenocrysts with resorbed cores of plagioclase ($An_{43–32}Ab_{53–63}Or_{3–5}$) mantled by oligoclase ($An_{23–25}Ab_{66–67}Or_{9–11}$) (Romengo *et al.*, 2012). The occurrence of such calcic compositions as cores suggests that the feldspars initially crystallized from magmas of intermediate composition and were being resorbed during subsequent melt evolution. It is possible that if the Montana Grande trachytes were part of the Green Tuff magma system (Mahood & Hildreth, 1986), benmoreitic magmas may have been trapped in these lower, dense and viscous levels in the chamber and could not rise into the part erupted as the Green Tuff. Many post-Green Tuff pantelleritic eruptive rocks have abundant trachytic enclaves (Prosperini *et al.*, 1990; Ferla & Meli, 2006; Landi & Rotolo, 2015), implying ready intrusion of trachyte to high levels. This suggests a remarkable efficiency for the trachyte 'trap' zone in the Green Tuff reservoir. It may be noted that Mattia *et al.* (2007) suggested that trapping of benmoreitic and mugearitic magmas in the chamber occurred as a result of their relatively high density compared with the more peralkaline rocks and contributed to the high values of the Bouguer anomaly.

Possible relationships in the plumbing system prior to the eruption of the Green Tuff are shown in Fig. 17. The upper part of the erupted reservoir is compositionally zoned pantellerite magma, underlain by feldspar-phyric trachyte. The crystal-rich colourless layer would be erupted during resurgence as the Montagna Grande lavas. The gabbroic mush represents the source of the trachytic magmas, squeezed out by either compaction or buoyancy.

CONCLUSIONS

(1) The Green Tuff was erupted from a magma reservoir compositionally zoned from pantellerite (top) to comenditic trachyte (bottom). Conditions within the reservoir are estimated to have been temperature ~900–700°C, fO_2 FMQ –1·5 to FMQ –0·5 and $aSiO_2$ (relative to quartz saturation) 0·74–1·00.

(2) The trachytic layer was rich in alkali feldspar phenocrysts and overlay the densely phyric Montagna Grande Trachyte, which was erupted during resurgence of the caldera whose formation accompanied eruption of the Green Tuff.

(3) Prior to eruption, the Green Tuff magma was layered by crystal fractionation of alkali feldspar–olivine–clinopyroxene–Fe–Ti oxide–apatite assemblages.

(4) During eruption, mingling between layers, especially in the pantellerites, was ubiquitous, at scales down to the micron level, a process revealed only by detailed analysis of within-sample glasses. Whole-rock analyses mask the significance of the mixing.

(5) The new glass analyses have significantly extended the range of melt compositions in the tuff, to those approaching the effective minimum composition for peralkaline silicic melts of Macdonald *et al.* (2012).

(6) Phenocrysts in the comenditic trachyte are commonly heavily resorbed but only slightly zoned compositionally, indicating perhaps that they were heated by, but did not mix with, influxes of intermediate magmas that were trapped in a lower layer.

ACKNOWLEDGEMENTS

We thank Lidia Jeżak for help with the electron microprobe analyses. Wes LeMasurier, David Neave, Silvio Rotolo and Editor Gerhard Wörner provided extremely detailed and helpful reviews of the paper.

SUPPLEMENTARY DATA

Supplementary data for this paper are available at *Journal of Petrology* online.

REFERENCES

Andersen, D. J. & Lindsley, D. H. (1988). Internally consistent solution models for Fe–Mg–Mn–Ti oxides. *American Mineralogist* **73**, 714–726.

Andersen, D. J., Lindsley, D. H. & Davidson, P. M. (1993). QUILF: a PASCAL program to assess equilibria among Fe–Mg–Mn–Ti oxides, pyroxenes, olivine, and quartz. *Computers and Geosciences* **19**, 1333–1350.

Avanzinelli, R., Bindi, L., Menchetti, S. & Conticello, S. (2004). Crystallization and genesis of peralkaline magmas from Pantelleria Volcano, Italy: an integrated petrological and crystal-chemical study. *Lithos* **73**, 41–69.

Bachmann, O. & Bergantz, G. W. (2008). Deciphering magma chamber dynamics from styles of compositional zoning in large silicic ash flow sheets. In: Putirka, K. D. & Tepley, F. J., III (eds) *Minerals, Inclusions and Volcanic Processes. Mineralogical Society of America and Geochemical Society, Reviews in Mineralogy and Geochemistry* **69**, 651–674.

Bacon, C. R. & Druitt, T. H. (1988). Compositional evolution of the zoned calcalkaline magma chamber of Mount Mazama, Crater Lake, Oregon. *Contributions to Mineralogy and Petrology* **98**, 224–256.

Bagiński, B., Macdonald, R., White, J. C. & Jeżak, L. (2018). Tuhualite in a peralkaline rhyolitic ignimbrite from Pantelleria, Italy. *European Journal of Mineralogy*. doi: 10.1127/ejm/2018/0030-2711.

Baker, B. H. & Henage, I. F. (1977). Compositional changes during crystallization of some peralkaline silicic lavas of the Kenya Rift Valley. *Journal of Volcanology and Geothermal Research* **2**, 17–28.

Behncke, B., Berrino, G., Corrado, G. & Velardita, R. (2006). Ground deformation and gravity changes on the island of Pantelleria in the geodynamic framework of the Sicily Channel. *Journal of Volcanology and Geothermal Research* **150**, 146–162.

Blake, S. (1981). Eruptions from zoned magma chambers. *Journal of the Geological Society, London* **138**, 281–287.

Blake, S. & Ivey, G. N. (1986). Magma mixing and the dynamics of withdrawal from stratified reservoirs. *Journal of Volcanology and Geothermal Research* **27**, 153–178.

Bohrson, W. A. & Reid, M. R. (1987). Genesis of silicic eralkaline volcanic rocks in an ocean island setting by crustal melting and pen-system processes: Socorro Island, Mexico. *Journal of Petrology* **38**, 1137–1166.

Bottinga, Y. & Weill, D. F. (1970). Densities of liquid silicate systems calculated from partial molar volumes of oxide components. *American Journal of Science* **269**, 169–182.

Calò, M. & Parisi, L. (2014). Evidences of a lithospheric fault zone in the Sicily Channel continental rift (southern Italy) from instrumental seismicity data. *Geophysical Journal International* **199**, 219–225.

Carmichael, I. S. E. (1991). The redox states of basic and silicic magmas: a reflection of their source regions? *Contributions to Mineralogy and Petrology* **106**, 129–141.

Carmichael, I. S. E. & Mackenzie, W. S. (1963). Feldspar–liquid equilibria in pantellerites: an experimental study. *American Journal of Science* **261**, 382–396.

Catalano, S., Tortorici, L. & Viccaro, M. (2014). Regional tectonic control on large size explosive eruptions: insights into the Green Tuff ignimbrite unit of Pantelleria. *Journal of Geodynamics* **73**, 23–233.

Chapman, D. S. & Pollack, H. N. (1975). Global heat flow: a new look. *Earth and Planetary Science Letters* **28**, 23–32.

Civetta, L., Cornette, Y., Crisci, G., Gillot, P. Y., Orsi, G. & Requejo, C. S. (1984). Geology, geochronology and chemical evolution of the island of Pantelleria. *Geological Magazine* **121**, 541–562.

Civetta, L., Cornette, Y., Gillot, P. Y. & Orsi, G. (1988). The eruptive history of Pantelleria (Sicily Channel) in the last 50 ka. *Bulletin of Volcanology* **50**, 47–57.

Civetta, L., D'Antonio, M., Orsi, G. & Tilton, G. R. (1998). The geochemistry of volcanic rocks from Pantelleria island, Sicily channel: petrogenesis and characteristics of the mantle source region. *Journal of Petrology* **39**, 1453–1491.

Civile, D., Lodolo, E., Tortorici, L., Lanzafame, G. & Brancolini, G. (2008). Relationships between magmatism and tectonics in a continental rift: the Pantelleria Island region (Sicily Channel, Italy). *Marine Geology* **251**, 32–46.

Della Vedova, B., Lucazeau, F., Pasquale, V., Pellis, G. & Verdoya, M. (1995). Heat flow in the tectonic provinces crossed by the southern segment of the European Geotraverse. *Tectonophysics* **244**, 57–74.

Di Carlo, I., Rotolo, S., Scaillet, B., Buccheri, V. & Pichavant, M. (2010). Phase equilibrium constraints on pre-eruptive conditions of recent explosive volcanism of Pantelleria Island, Italy. *Journal of Petrology* **51**, 2245–2276.

D'Oriano, C., Landi, P., Pimentel, A. & Zanon, V. (2017). Magmatic processes revealed by anorthoclase textures and trace element modelling: the case of the Lajes Ignimbrite eruption (Terceira Island, Azores). *Journal of Volcanology and Geothermal Research* **347**, 44–63.

Esperança, S. & Crisci, G. M. (1995). The island of Pantelleria: a case for the development of DMM–HIMU isotopic

compositions in a long-lived extensional setting. *Earth and Planetary Science Letters* **136**, 167–182.

Ferla, P. & Meli, C. (2006). Evidence of magma mixing in the 'Daly Gap' of alkaline suites: a case study from the enclaves of Pantelleria (Italy). *Journal of Petrology* **47**, 1467–1502.

Flude, S., Burgess, R. & McGarvie, D. W. (2008). Silicic volcanism at Ljósufjöll, Iceland: insights into evolution and eruptive history from Ar–Ar dating. *Journal of Volcanology and Geothermal Research* **169**, 154–175.

Forni, F., Petricca, E., Bachmann, O., Mollo, S., De Astis, G. & Piochi, M. (2018). The role of magma mixing/mingling and cumulate melting in the Neapolitan Yellow Tuff caldera-forming eruption (Campi Flegrei, Southern Italy). *Contributions to Mineralogy and Petrology* **173**, 45.

Frost, B. R., Lindsley, D. H. & Andersen, D. J. (1988). Fe–Ti oxide–silicate equilibria: assemblages with fayalitic olivine. *American Mineralogist* **73**, 727–740.

Fulignati, P., Malfitano, G. & Sbrana, A. (1997). The Pantelleria caldera geothermal system: data from the hydrothermal minerals. *Journal of Volcanology and Geothermal Research* **75**, 251–270.

Gantar, C., Morelli, C., Segre, A. & Zampieri, L. (1961). Studio gravimetrico e considerazioni geologiche sull'isola di Pantelleria. *Bollettino Geofisica Teorica ed Applicata* **3**, 267–287.

Gioncada, A. & Landi, P. (2010). The pre-eruptive volatile contents of recent basaltic and pantelleritic magmas at Pantelleria (Italy). *Journal of Volcanology and Geothermal Research* **189**, 191–201.

Jeffery, A. J., Gertisser, R., Self, S., Pimentel, A., O'Driscoll, B. & Pacheco, J. M. (2017). Petrogenesis of the peralkaline ignimbrites of Terceira, Azores. *Journal of Petrology* **58**, 2365–2402.

Jordan, N. J., Rotolo, S. G., Williams, R., Speranza, F., McIntosh, W. C., Branney, M. J. & Scaillet, S. (2018). Explosive eruptive history of Pantelleria, Italy: repeated caldera collapse and ignimbrite emplacement at a peralkaline volcano. *Journal of Volcanology and Geothermal Research* **349**, 47–73.

Korringa, M. K. & Noble, D. C. (1972). Genetic significance of chemical, isotopic, and petrographic features of some peralkaline salic rocks from the island of Pantelleria. *Earth and Planetary Science Letters* **17**, 258–262.

Kovalenko, V. I., Naumov, V. B., Solovova, I. P., Girnis, A. V., Hervig, R. L. & Boriani, A. (1994). Volatile components, composition, and crystallization conditions of the Pantelleria basalt–pantellerite association magmas, inferred from the melt and fluid inclusion data. *Petrology* **2**, 19–34.

Kunzmann, T. (1999). The aenigmatite–rhönite mineral group. *European Journal of Mineralogy* **11**, 743–756.

Landi, P. & Rotolo, S. G. (2015). Cooling and crystallization recorded in trachytic enclaves hosted in pantelleritic magmas (Pantelleria, Italy): implications for pantellerite petrogenesis. *Journal of Volcanology and Geothermal Research* **301**, 169–179.

Lanzo, G., Landi, P. & Rotolo, S. G. (2013). Volatiles in pantellerite magmas: a case study of the Green Tuff Plinian eruption (Island of Pantelleria). *Journal of Volcanology and Geothermal Research* **262**, 153–163.

Le Maitre, R. W. (ed.) (2002). *A Classification of Igneous Rocks and Glossary of Terms. Recommendations of the International Union of Geological Sciences Subcommission on the Systematics of Igneous Rocks*, 2nd edn. Cambridge: Cambridge University Press.

Lowenstern, J. B. (1994). Chlorine, fluid immiscibility, and degassing in peralkaline magmas from Pantelleria, Italy. *American Mineralogist* **79**, 353–369.

Lowenstern, J. B. & Mahood, G. A. (1991). New data on magmatic H_2O contents of pantellerites, with implications for petrogenesis and eruptive dynamics at Pantelleria. *Bulletin of Volcanology* **54**, 78–83.

Macdonald, R. (1974). Nomenclature and petrochemistry of the peralkaline oversaturated extrusive rocks. *Bulletin Volcanologique* **38**, 498–516.

Macdonald, R. & Scaillet, B. (2006). The central Kenya peralkaline province: Insights into the evolution of peralkaline salic magmas. *Lithos* **91**, 59–73.

Macdonald, R., Navarro, J. M., Upton, B. G. J. & Davies, G. R. (1994). Strong compositional zonation in peralkaline magma: Menengai, Kenya Rift Valley. *Journal of Volcanology and Geothermal Research* **60**, 301–325.

MacDonald, R., Baginński, B., Belkin, H. E., Dzierżanowski, P. & Jeżak, L. (2008). Compositional variations in apatite from a benmoreite–peralkaline rhyolite volcanic suite, Kenya Rift Valley. *Mineralogical Magazine* **72**, 1147–1161.

Macdonald, R., Bagiński, B., Leat, P. T., White, J. C. & Dzierżanowski, P. (2011). Mineral stability in peralkaline silicic rocks: information from trachytes of the Menengai volcano, Kenya. *Lithos* **125**, 553–568.

Macdonald, R., Bagiński, B., Ronga, F., Dzierżanowski, P., Lustrino, M., Marzoli, A. & Melluso, L. (2012). Evidence for extreme fractionation of peralkaline silicic magmas, the Boseti volcanic complex, Main Ethiopian Rift. *Mineralogy and Petrology* **104**, 163–175.

Mahood, G. A. (1984). Pyroclastic rocks and calderas associated with strongly peralkaline magmatism. *Journal of Geophysical Research* **89**, 8540–8552.

Mahood, G. A. & Baker, D. R. (1986). Experimental constraints on depths of fractionation of mildly alkalic basalts and associated felsic rocks: Pantelleria, Strait of Sicily. *Contributions to Mineralogy and Petrology* **93**, 251–264.

Mahood, G. A. & Hildreth, W. (1986). Geology of the peralkaline volcano at Pantelleria, Strait of Sicily. *Bulletin of Volcanology* **48**, 143–172.

Mahood, G. A. & Stimac, J. A. (1990). Trace-element partitioning in pantellerites and trachytes. *Geochimica et Cosmochimica Acta* **54**, 2257–2276.

Margari, V., Pyle, D. M., Bryant, C. & Gibbard, P. L. (2007). Mediterranean tephra stratigraphy revisited: results from a long terrestrial sequence on Lesvos Island, Greece. *Journal of Volcanology and Geothermal Research* **163**, 34–54.

Mattia, M., Bonaccorso, A. & Guglielmino, F. (2007). Ground deformations in the Island of Pantelleria (Italy): insights into the dynamics of the current intereruptive period. *Journal of Geophysical Research* **112**, B11406.

Morelli, C., Gantar, C. & Pisani, M. (1975). Bathymetry, gravity and magnetism in the Straits of Sicily and Ionian Sea. *Bollettino di Geofisica Teorica ed Applicata* **17**, 39–58.

Mungall, J. E. & Martin, R. F. (1995). Petrogenesis of basalt–comendite and basalt–pantellerite suites, Terceira, Azores, and some implications for the origin of ocean-island rhyolites. *Contributions to Mineralogy and Petrology* **119**, 43–55.

Neave, D. A., Fabbro, G., Herd, R. A., Petrone, C. M. & Edmonds, M. (2012). Melting, differentiation and degassing at the Pantelleria volcano, Italy. *Journal of Petrology* **53**, 637–663.

Noble, D. C. (1967). Sodium, potassium, and ferrous iron contents of some secondarily hydrated natural silicic glasses. *American Mineralogist* **52**, 280–286.

Noble, D. C. (1970). Loss of sodium from crystallized comendite welded tuffs of the Miocene Grouse Canyon Member of the Belted Range Tuff, Nevada. *Geological Society of America Bulletin* **81**, 2677–2687.

Noble, D. C., Smith, V. C. & Peck, L. C. (1967). Loss of halogens from crystallized and glassy silicic volcanic rocks. *Geochimica et Cosmochimica Acta* **31**, 215–223.

Orsi, G. & Sheridan, M. F. (1984). The Green Tuff of Pantelleria: rheoignimbrite or rheomorphic fall? *Bulletin Volcanologique* **47**, 611–626.

Orsi, G., Gallo, G. & Zanchi, A. (1991). Simple-shearing block resurgence in caldera depressions. A model from Pantelleria and Ischia. *Journal of Volcanology and Geothermal Research* **47**, 1–11.

Parker, D. F. & White, J. C. (2008). Large-scale alkali magmatism associated with the Buckhorn caldera, Trans-Pecos Texas, USA: comparison with Pantelleria, Italy. *Bulletin of Volcanology* **70**, 403–415.

Pimentel, A., Zanon, V., de Groot, L. V., Hipólito, A., Di Chiara, A. & Self, S. (2016). Stress-induced comenditic trachyte effusion triggered by trachybasalt intrusion: multidisciplinary study of the AD 1761 eruption at Terceira Island (Azores). *Bulletin of Volcanology* **78**, 22.

Pouchou, J. L. & Pichoir, J. F. (1991). Quantitative analysis of homogeneous or stratified microvolumes applying the model 'PAP'. In: Heinrich, K. F. J. & Newbury, D. E. (eds) *Electron Probe Quantification.* New York: Plenum, pp. 31–75.

Prosperini, N., Perugini, D., Poli, G. & Manetti, P. (1990). Magmatic enclaves distribution within the Khaggiar lava dome (Pantelleria, Italy): implications for magma chamber dynamics and eruption. *Acta Vulcanologica* **12**, 37–47.

Putirka, K. D., Mikaelian, H., Ryerson, F. & Shaw, H. (2003). New clinopyroxene–liquid thermobarometers for mafic, evolved, and volatile-bearing lava compositions, with applications to lavas from Tibet and the Snake River Plain, Idaho. *American Mineralogist* **88**, 1542–1554.

Romano, P., White, J. C., Ciulla, A., Di Carlo, I., D'Oriano, C., Landi, P. & Rotolo, S.G. (2019). Volatile and trace element contents in melt inclusions from the zoned Green Tuff ignimbrite (Pantelleria): petrological inferences. *Annals of Geophysics*, in press.

Romano, P., Andújar, J., Scaillet, B., Romengo, N., di Carlo, I. & Rotolo, S. G. (2018). Phase equilibria of Pantelleria trachytes (Italy): constraints on pre-eruptive conditions and on the metaluminous to peralkaline transition in silicic magmas. *Journal of Petrology* **59**, 559–588.

Romengo, N., Landi, P. & Rotolo, S. G. (2012). Evidence of basaltic magma intrusions in a trachytic magma chamber at Pantelleria (Italy). *Periodico di Mineralogia* **81**, 163–178.

Sack, R. O., Carmichael, I. S. E., Rivers, M. & Ghiorso, M. S. (1980). Ferric–ferrous equilibria in natural silicate liquids at 1 bar. *Contributions to Mineralogy and Petrology* **75**, 369–376.

Scaillet, B. & Macdonald, R. (2001). Phase relations of peralkaline silicic magmas and petrogenetic implications. *Journal of Petrology* **42**, 825–845.

Scaillet, B. & Macdonald, R. (2003). Experimental constraints on the relationships between peralkaline rhyolites of the Kenya Rift Valley. *Journal of Petrology* **44**, 1867–1894.

Scaillet, B. & Macdonald, R. (2006). Experimental constraints on pre-eruptive conditions of pantelleritic magmas: evidence from the Eburru complex, Kenya Rift. *Lithos* **91**, 95–108.

Scaillet, S., Rotolo, S. G., La Felice, S. & Vita-Scaillet, G. (2011). High-resolution $^{40}Ar/^{39}Ar$ chronostratigraphy of the post-caldera (<20 ka) volcanic activity at Pantelleria, Sicily Strait. *Earth and Planetary Science Letters* **309**, 280–290.

Scaillet, S., Vita-Scaillet, G. & Rotolo, S. G. (2013). Millenial-scale phase relationships between ice-core and Mediterranean marine records: insights from high-precision $^{40}Ar/^{39}Ar$ dating of the Green Tuff of Pantelleria, Sicily Strait. *Quaternary Science Reviews* **78**, 141–154.

Schuraytz, B. C., Vogel, T. A. & Younker, L. W. (1989). Evidence for dynamic withdrawal from a layered magma body: the Topopah Spring Tuff, southwestern Nevada. *Journal of Geophysical Research* **94**, 5925–5942.

Spera, F. J., Yuen, D. A., Greer, J. C. & Sewell, G. (1986). Dynamics of magma withdrawal from stratified magma chambers. *Geology* **14**, 723–726.

Sumner, J. M. & Wolff, J. (2003). Petrogenesis of mixed-magma, high-grade, peralkaline ignimbrite 'TL' (Gran Canaria): diverse styles of mixing in a replenished, zoned magma chamber. *Journal of Volcanology and Geothermal Research* **126**, 109–126.

Sun, S.-S. & McDonough, W. F. (1989). Chemical and isotopic systematics of oceanic basalts: implications for mantle composition and processes. In: Saunders, A. D., & Norry, M. J. (eds) *Magmatism in the Ocean Basins. Geological Society, London, Special Publications* **42**, 313–345.

Troll, V. R. & Schmincke, H.-U. (2002). Magma mixing and crustal recycling recorded in ternary feldspar from compositionally zoned peralkaline ignimbrite 'A', Gran Canaria, Canary Islands. *Journal of Petrology* **43**, 243–270.

Verzhbitsky, E. V. & Kononov, M. V. (2003). Heat flow and origin of the lithosphere in the central Mediterranean region. *Geotectonics* **37**, 328–336.

Villari, L. (1974). The island of Pantelleria. *Bulletin Volcanologique* **38**, 680–724.

Weaver, S. D., Gibson, I. L., Houghton, B. F. & Wilson, C. J. N. (1990). Mobility of rare earth and other elements during crystallization of peralkaline silicic lavas. *Journal of Volcanology and Geothermal Research* **43**, 57–70.

White, J. C., Holt, G. S., Parker, D. F. & Ren, M. (2003). Trace-element partitioning between alkali feldspar and peralkalic quartz trachyte to rhyolite magma. Part 1: systematics of trace-element partitioning. *American Mineralogist* **88**, 316–329.

White, J. C., Ren, M. & Parker, D. F. (2005). Variation in mineralogy, temperature, and oxygen fugacity in a suite of strongly peralkaline lavas and tuffs, Pantelleria, Italy. *Canadian Mineralogist* **43**, 1331–1347.

White, J. C., Parker, D. F. & Ren, M. (2009). The origin of trachyte and pantellerite from Pantelleria, Italy: insights from major element, trace element, and thermodynamic modelling. *Journal of Volcanology and Geothermal Research* **179**, 33–55.

Williams, R., Branney, M. J. & Barry, T. L. (2014). Temporal and spatial evolution of a waxing then waning catastrophic density current revealed by chemical mapping. *Geology* **42**, 107–110.

Wolff, J. A. & Wright, J. V. (1981). Formation of the Green Tuff, Pantelleria. *Bulletin Volcanologique* **44**, 681–690.

Wright, J. V. (1980). Stratigraphy and geology of the welded air-fall tuffs of Pantelleria. *Geologische Rundschau* **69**, 263–291.

APPENDIX

Table A1: Details of analyzed samples

		Geographical coordinates		UTM (Zone 32S)		Location
Sample ID	Rock type	Lat. (°N)	Long. (°E)	mE	mN	
150511	eutaxitic lapilli tuff	36·76836	11·96072	764264	4073266	Punta Tre Pietre
150513	rheomorphic tuff	36·76811	11·95942	764147	4073234	Punta Tre Pietre
150514	eutaxitic lapilli tuff	36·77172	11·95600	763831	4073626	Punta Tre Pietre
150521	glassy eutaxitic tuff	36·77378	11·97467	765489	4073904	Monastero Scarp
150522	top of deposit	36·76689	11·98311	766269	4073164	Monastero Scarp
150534	glassy top of section	36·78792	11·94808	763069	4075401	Contrada Scirafi
150541	fall deposit(?)	36·81133	11·97583	765465	4078078	Zinedi Scarp
150542	lower pumice	36·81992	11·99858	767465	4079092	Cinque Denti Scarp
150543	fiamme bed	36·81986	11·99817	767427	4079085	Cinque Denti Scarp
150544	basal bomb bed	36·82425	11·98381	766133	4079530	Khartibucale Scarp
150546	vitrophyric base	36·82456	11·98522	766257	4079570	Khartibucale Scarp
150551	glassy base of deposit	36·83511	11·96942	764811	4080699	Punta della Guarda
160541	densely welded tuff	36·77375	11·97465	765489	4073902	Monastero Scarp
160542	glassy upper unit	36·77423	11·97454	765477	4073955	Monastero Scarp
160543	eutaxitic lapilli tuff	36·77479	11·97427	765451	4074017	Monastero Scarp

Datum for all coordinates is WGS84.